Applied Mathematical Modelling 130 (2024) 827–851

Contents lists available at ScienceDirect

Applied Mathematical Modelling

journal homepage: www.elsevier.com/locate/apm

An analytical investigation into solute transport and sorption via intra-particle diffusion in the dual-porosity limit

Lucy C. Auton [a], Maria Aguareles [b,*], Abel Valverde [c,d], Timothy G. Myers [a], Marc Calvo-Schwarzwalder [e]

[a] Centre de Recerca Matemàtica, Campus de Bellaterra, Edifici C, 08193 Bellaterra, Barcelona, Spain
[b] Department of Computer Science, Applied Mathematics and Statistics, Universitat de Girona, Campus de Montilivi, 17071 Girona, Catalunya, Spain
[c] Universitat Politècnica de Catalunya, Barcelona, Spain
[d] Visiting Fellow, Mathematical Institute, University of Oxford, Oxford, United Kingdom
[e] College of Interdisciplinary Studies, Zayed University, P.O. Box 144534, Abu Dhabi, United Arab Emirates

ARTICLE INFO

Dataset link: https://github.com/aguareles/Intra-particle-diffusion

MSC:
35Q35
35B40

Keywords:
Contaminant removal
Adsorption
Advection-diffusion
Mathematical analysis
Asymptotics

ABSTRACT

We develop a mathematical model for adsorption based on averaging the flow around, and diffusion inside, adsorbent particles in a column. The model involves three coupled partial differential equations for the contaminant concentration both in the carrier fluid and within the particle as well as the adsorption rate. The adsorption rate is modelled using the Sips equation, which is suitable for describing both physical and chemical adsorption mechanisms. Non-dimensionalisation is used to determine the controlling parameter groups as well as to determine negligible terms and so reduce the system complexity. The inclusion of intra-particle diffusion introduces new dimensionless parameters to those found in standard works, including a form of internal Damköhler number and a new characteristic time scale. We provide a numerical method for the full model and show how in certain situations a travelling wave approach can be utilized to find analytical solutions. The model is validated against published experimental data for the removal of Mercury(II) and CO_2. The results show excellent agreement with measurements of column outlet contaminant concentration and provide insights into the underlying chemical reactions.

1. Introduction

Column sorption is a popular practical sorption method and is used for a wide range of processes, such as the removal of emerging contaminants, volatile organic compounds, CO_2, dyes and salts. With this technique, pollutants are removed from a fluid by letting the mixture flow through a column filled with a porous material, the adsorbent, which captures the contaminant. The mathematical description of these processes may be traced back to the 20th century and the most commonly used model is that of Bohart and Adams [1]. Recently, the validity and physical accuracy of this model have been discussed [2–7] highlighting a need for mathematical descriptions that better describe the underlying physical and chemical processes.

Many sorption filters may be described as dual-porosity filters, *i.e.*, they comprise an array of grains each of which is itself porous. This leads to two distinct regions: the 'inter-particle' region (between the grains) and the 'intra-particle' region (within each porous

* Corresponding author.
E-mail address: maria.aguareles@udg.edu (M. Aguareles).

https://doi.org/10.1016/j.apm.2024.03.023
Received 16 November 2023; Received in revised form 22 March 2024; Accepted 27 March 2024

Available online 3 April 2024

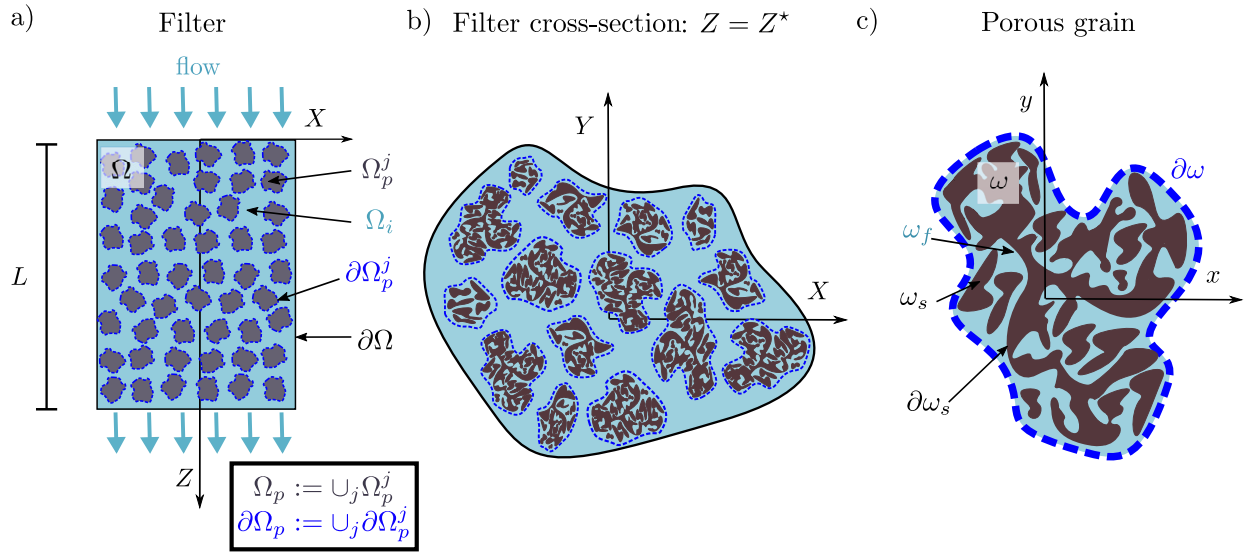

Fig. 1. Flow of fluid carrying solute through a dual-porosity filter. (a) The fluid travels in the Z direction with the inlet defined by $Z = 0$ and outlet by $Z = L$, (b) the cross-section of the arbitrarily shaped filter is spanned by the X-Y plane. (c) Within any given identical but arbitrarily shaped three-dimensional grain, positions are determined via a local (x, y, z) coordinate system.

grain). This distinction is neglected in standard models, where it is assumed that the adsorbate (*i.e.*, the contaminant once adsorbed) immediately attaches to the adsorbent. However, as the size of the adsorbing particles increases (for example, as the scale of the process is increased from experimental to industrial scale) it is clear that the intermediate step where the contaminant first diffuses into the adsorbent and then attaches to its inner surface has to be accounted for. This observation is supported by the recorded differences in qualitative behaviour of the breakthrough curves (the contaminant concentration at the column outlet) as the particle size increases [4,8].

A classic kinetic model for adsorption is attributed to Langmuir [9] and it is based on the assumption that the underlying mechanism is caused by the attraction between a monolayer of adsorbate and the available sites on the surface of the adsorbent (physisorption). The rate of adsorption is then proportional to the contaminant concentration and available sites. In practice, many adsorbents remove contaminants via a chemical reaction (chemisorption). If the chemical reaction is such that one molecule of contaminant reacts with one molecule of adsorbent then the Langmuir model also proves effective. However, in reality these chemical reactions can often be more complex, involving a chain of chemical reactions or a non one-to-one relation between the number of molecules of adsorbent and number of molecules of contaminant. A model proposed for these cases is the Sips model [10], which has two parameters that depend on the underlying chemistry (on the global order of the reaction) within the system.

In the context of physical adsorption and intra-particle diffusion, Mondal et al. [11] propose a model that is applied to the removal of arsenic from drinking water in India, but the averaging process conducted there shows some inconsistencies that have been recently addressed by Valverde et al. [4]. Seidensticker et al. [12] present an intra-particle diffusion model for investigating the potential of microplastics to adsorb and transport contaminants. In the present paper, we propose a model to account for chemical adsorption utilizing the Sips model, which has been shown to provide accurate results for small particles, when intra-particle diffusion is negligible [13]. This is particularly interesting as this kinetic model reduces to more standard ones, such as the Langmuir or Freundlich models, in certain limits. To support the mass transfer model developed in Valverde et al. [4], we re-develop the mathematical description with a higher degree of mathematical rigor while simultaneously extending the model to account for porous grains of arbitrary shape and coupling the intra-particle model to the Sips model, rather than Langmuir's model.

This article is structured as follows. In §2 we develop a macroscopic model based on a series of averages of microscopic variables, and discuss the related dimensionless parameters. In §3 we investigate numerical and semi-analytical solutions for physically realistic parameter combinations using a travelling wave approach. Further, we provide general results that determine in which situations such travelling wave solutions exist. The analytical expressions are validated against experimental data in §4. Finally, §5 contains the conclusions and thoughts on possible future research.

2. Model problem

We consider the flow of fluid carrying a solute through a rigid porous cylinder of length L. The solute advects, diffuses, and is removed via adsorption to the solid structure (the adsorbent). The spatial coordinate within the cylinder is $\boldsymbol{X} := (X, Y, Z)^\intercal$ with Z the longitudinal coordinate and X and Y are the coordinates in the plane of the cross-section (see Fig. 1a,b). The fluid enters the porous medium uniformly through the inlet, at $Z = 0$, and exits at $Z = L$.

The entire domain of the porous medium, denoted Ω, comprises an array of N identical but arbitrarily shaped porous grains. Within any porous grain we define a local spatial co-ordinate $\boldsymbol{x} := (x, y, z)^{\mathsf{T}}$ (Fig. 1c). Note that although every grain is identical, when taking a cross-section the plane of intersection can contain obstacles of different sizes and shapes.

The solute molecules are assumed to be much smaller than the solid obstacles. We measure the local molar concentration of solute (amount of solute per volume of fluid *surrounding the porous grains*) via the inter-particle concentration field $c(\boldsymbol{X}, t)$, measured in moles/m^3. This is defined over the inter-particle fluid domain, denoted Ω_i, and we impose that $c(\boldsymbol{X}, t) \equiv 0$ inside the porous grains. We denote the domain comprising the union of all porous grains as $\Omega_p := \Omega \setminus \Omega_i \equiv \bigcup \Omega_p^j$, where Ω_p^j denotes the domain of the j^{th} porous grain (Fig. 1a).

As we have both local and global spatial coordinates, $\boldsymbol{x}$ and $\boldsymbol{X}$, respectively, we also define the domain of any porous grain relative to $\boldsymbol{x}$ to be ω so that $\boldsymbol{x} \in \omega \equiv X \in \Omega_p^j$, for some j. Each porous grain is bounded by a fluid-fluid interface which is a smooth surface $\partial\omega$ that is the enclosure of the porous grain (see Fig. 1c). We denote the local molar concentration of solute (amount of solute per volume of fluid *contained within a given grain*) via the intra-particle concentration field $c_p^j(\boldsymbol{x}, \boldsymbol{X}, t)$, measured in moles/m^3, which is defined within the internal fluid region denoted ω_f. We extend the definition of c_p^j across the entire porous particle domain by enforcing that $c_p^j \equiv 0$ in $\omega_s := \omega \setminus \omega_f$, that is the solid domain in the particle.

We track how much solute adsorbs to the j^{th} porous grain via a mass sink $M_p^j(\boldsymbol{X}, t)$, measured in moles, however, we neglect any impact of this adsorption on the size and volume of the solid, that is, we take ω_s, and consequently every domain, to be independent of time. This is justified by the fact that the solute molecules are negligible in size relative to the obstacles and also because in this work the fluids under consideration are assumed to have low contaminant concentrations.

We define the total porosity of the cylinder to be Φ, that is, the void fraction of the porous material which comprises both the void space between the grains and the void space within each grain. We take the average porosity within any grain to be the same and define this value to be the 'intra-particle' porosity $\phi_p := |\omega_f|/|\omega|$, for all j. Finally, we define the 'inter-particle' porosity $\phi := |\Omega_i|/|\Omega|$ to be the value that would be calculated if the grains had zero porosity (*i.e.*, $\phi \equiv \Phi \iff \phi_p = 0$). Thus we relate Φ, ϕ_p and ϕ via

$$1 - \Phi \equiv (1 - \phi)(1 - \phi_p)\,. \tag{1}$$

2.1. Full model

We now derive equations for both the inter-particle concentration of adsorbate, $c(\mathbf{X}, t)$ and the intra-particle concentration, $c_p^j(\boldsymbol{x}, \boldsymbol{X}, t)$.

2.1.1. Inter-particle model

In the inter-particle region we model the flow as unidirectional and uniform along the length of the cylinder, that is, we take a constant Darcy flux $\boldsymbol{Q} := \Phi v \boldsymbol{e}_Z$ such that v is the average interstitial velocity of the fluid and where $\boldsymbol{e}_Z$ is the unit vector along the length of the filter. The transport is then described by an advection-diffusion equation

$$\frac{\partial c}{\partial t} + \frac{\partial}{\partial Z}(vc) = \boldsymbol{\nabla}_{\boldsymbol{X}} \cdot \left(\mathfrak{D} \cdot \boldsymbol{\nabla}_{\boldsymbol{X}} c\right), \quad \boldsymbol{X} \in \Omega_i\,, \tag{2a}$$

where

$$\mathfrak{D}(\boldsymbol{X}) := \begin{pmatrix} D_{11}(\boldsymbol{X}) & D_{12}(\boldsymbol{X}) & 0 \\ D_{21}(\boldsymbol{X}) & D_{22}(\boldsymbol{X}) & 0 \\ 0 & 0 & D \end{pmatrix} = \begin{pmatrix} \mathfrak{D}^{X,Y}(\boldsymbol{X}) & 0 \\ 0 & D \end{pmatrix}, \tag{2b}$$

is the effective diffusivity tensor and where $\boldsymbol{\nabla}_{\boldsymbol{X}}$ is the gradient vector with respect to the spatial coordinate $\boldsymbol{X}$. Note that $\mathfrak{D}$ comprises contributions from molecular diffusion, Taylor or shear dispersion, and turbulent mixing; we allow for shear in the in plane components of $\mathfrak{D}$ and further allow for dependence on $\boldsymbol{X}$ but we take the longitudinal component to be a purely unidirectional constant whose value is an experimentally determined average. That the predominant flow is in the axial direction is a standard assumption in the field. It may be verified through the work of Mondal et al. [11] who use the Darcy-Brinkman approximation to permit the inclusion of radial flow in column adsorption. They obtained a Darcy number of the order 10^{-7}, so confirming that the flow was predominantly unidirectional, except for in a very narrow boundary layer at the column walls.

The condition at the impermeable wall of the cylinder, $\partial\Omega$, reads

$$\left(\mathfrak{D} \cdot \boldsymbol{\nabla}_{\boldsymbol{x}} c\right) \cdot \boldsymbol{n}_o = 0, \quad \boldsymbol{X} \in \partial\Omega, \tag{2c}$$

where $\boldsymbol{n}_o$ is the unit, outward-facing normal to $\partial\Omega$. At the fluid-fluid interface which bounds the porous grains, we enforce a mass balance between the inter- and intra-particle regions such that the mass transfer is determined by an empirical relation (discussed in §2.2). These conditions couple the inter-particle and intra-particle regions, thus before considering any conditions here, we present the problem in the intra-particle problem.

2.1.2. Intra-particle model

As stated we consider a dual-porosity limit, *i.e.*, there is a preferential flow path in the inter-particle domain. As such we assume that the flow, and consequently contaminant transport via advection, is negligible within the porous grains and so model the contaminant concentration c_p^j within each grain via a diffusive transport equation

$$\frac{\partial c_p^j}{\partial t} = \nabla_{\boldsymbol{x}} \cdot \left(\mathfrak{D}_p(\boldsymbol{x}) \cdot \nabla_{\boldsymbol{x}} c_p^j \right), \quad \boldsymbol{x} \in \omega_f, \quad \boldsymbol{X} \in \Omega_p^j, \tag{3}$$

where $\mathfrak{D}_p(\boldsymbol{x})$ is an effective diffusivity tensor and $\nabla_{\boldsymbol{x}}$ is the gradient vector with respect to the spatial coordinate $\boldsymbol{x}$. At the fluid-solid interface, $\partial\omega_s$, the adsorption reaction occurs

$$\int_{\partial\omega_s} \left(\mathfrak{D}_p(\boldsymbol{x}) \cdot \nabla_{\boldsymbol{x}} c_p^j \right) \cdot \boldsymbol{n}_s \mathrm{d}S_x = \frac{\partial M_p^j}{\partial t}, \quad \boldsymbol{X} \in \Omega_p^j, \tag{4}$$

where $\boldsymbol{n}_s$ is the outward facing unit normal to the solid in a porous grain, $\mathrm{d}S_x$ is the area element with respect to $\boldsymbol{x}$ and we recall that $M_p^j(\boldsymbol{X}, t)$ is the number of moles that have been adsorbed by the j^{th} porous grain. Equation (4) is then a mass flux balance through the surface ω_s; M_p^j will be specified based on the chemical behaviour of the system.

At the fluid-fluid interface $\partial\omega$, we apply a condition describing the total flux of mass F_j entering the j^{th} porous grain

$$\int_{\partial\omega} \left(\mathfrak{D}_p(\boldsymbol{x}) \cdot \nabla_{\boldsymbol{x}} c_p^j \right) \cdot \boldsymbol{n}_p \mathrm{d}S_x = F_j, \quad \boldsymbol{X} \in \Omega_p^j, \tag{5}$$

where $\boldsymbol{n}_p$ is the outward-facing unit normal to the porous grain. Here we leave the form of F_j unspecified, but we provide an expression in §2.2 when dealing with a simplified model. We later specify the functional form of F_j. Note that the same condition must apply in the interparticle region to ensure conservation of mass (see §2.2).

The aim of this model is to predict the macroscopic and filtration behaviour of materials. As such, we are not concerned with modelling the diffusive behaviour within a single grain but rather the effect of these grains on the macroscale filtration properties. Thus, we consider the intrinsic (fluid) average over a porous grain for a given quantity $\star = \star(\boldsymbol{x}, \boldsymbol{X}, t)$

$$\langle \star \rangle(\boldsymbol{X}, t) := \frac{1}{|\omega_f|} \int_{\omega_f} \star(\boldsymbol{x}, \boldsymbol{X}, t) \, \mathrm{d}V_x \equiv \frac{1}{\phi_p |\omega|} \int_{\omega_f} \star(\boldsymbol{x}, \boldsymbol{X}, t) \, \mathrm{d}V_x, \quad \boldsymbol{X} \in \Omega_p^j, \tag{6}$$

for some j, where $|\omega_f|$ is the total fluid volume in a given porous grain and where $\mathrm{d}V_x$ is a volume element in the intra-particle fluid region, with respect to $\boldsymbol{x}$. Taking the intrinsic average of Equation (3), applying the divergence theorem, and recalling that $c_p^j \equiv 0$ for $\boldsymbol{x} \in \omega_s$, yields

$$\begin{aligned} \frac{\partial \langle c_p^j \rangle}{\partial t} &= \frac{1}{|\omega_f|} \int_{\partial\omega_f} \left(\mathfrak{D}_p(\boldsymbol{x}) \cdot \nabla_{\boldsymbol{x}} c_p^j \right) \cdot \boldsymbol{n}_f \mathrm{d}S_x \\ &\equiv -\frac{1}{|\omega_f|} \int_{\partial\omega_s} \left(\mathfrak{D}_p(\boldsymbol{x}) \cdot \nabla_{\boldsymbol{x}} c_p^j \right) \cdot \boldsymbol{n}_s \mathrm{d}S_x + \frac{1}{|\omega_f|} \int_{\partial\omega} \left(\mathfrak{D}_p(\boldsymbol{x}) \cdot \nabla_{\boldsymbol{x}} c_p^j \right) \cdot \boldsymbol{n}_p \mathrm{d}S_x \\ &\equiv -\frac{1}{\phi_p |\omega|} \frac{\partial M_p^j}{\partial t} + \frac{F}{\phi_p |\omega|}, \quad \boldsymbol{X} \in \Omega_p^j, \end{aligned} \tag{7}$$

where $\boldsymbol{n}_f$ is the outward-facing unit normal to the fluid within a porous grain and where the last equality follows from the conditions (4) and (5). Note that by taking the intrinsic average over each porous grain, $\langle c_p^j \rangle$ is now independent of $\boldsymbol{x}$. We define the *extension* operator $E[y^j]$ to be

$$E[y^j] := \begin{cases} y^j, & \text{for} \quad \boldsymbol{X} \in \Omega_p^j, \quad j \in \{1, 2, \cdots, N\}, \\ 0, & \text{if} \quad \boldsymbol{X} \in \Omega_i, \end{cases} \tag{8}$$

leading to the piecewise extended version of the intra-particle concentration field, c_p, the removal sink, M_p, and the mass flux, F,

$$c_p(\boldsymbol{X}, t) = E\left[\langle c_p^j \rangle \right], \qquad M_p(\boldsymbol{X}, t) = E\left[M_p^j \right], \qquad F(\boldsymbol{X}, t) = E\left[F_j \right], \tag{9}$$

which are now defined over the whole domain Ω.

To close the problem we must prescribe the behaviour of the removal M_p and the mass flux F. This is carried out in the following section.

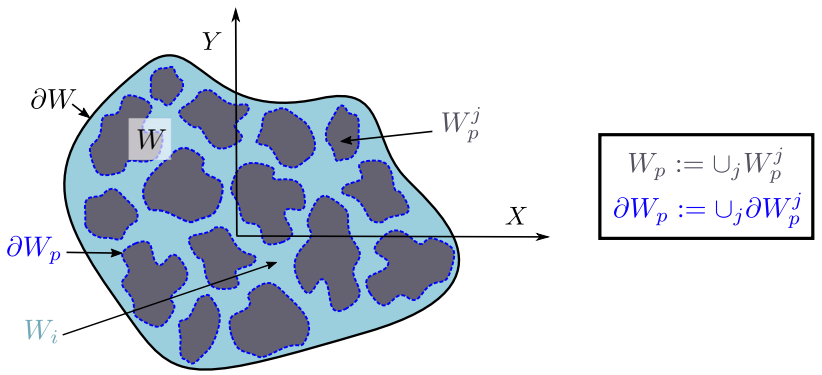

Fig. 2. Cross-section of the filter spanned by the X-Y plane.

2.2. Model simplification

The aim of this paper is to develop a simple model for flow and adsorption in a dual-porosity material. Consequently, we employ cross-sectional averaging over the macroscale which is inspired by an ensemble average [4,6,7]. This approach has previously shown good agreement with experimental data [4,13]. Mirroring the definitions of Ω we now define notation in an arbitrary two-dimensional cross-section of the filter $Z = Z^\star \in \Omega$: the inter-particle domain is denoted $W_i(Z^\star)$, the union of the distinct particle domains $(W_p^j(Z^\star))$ is denoted $W_p(Z^\star)$, with the domain of the entire cross-section denoted W with boundary ∂W (Fig. 2). Note that although W_p and W_i are functions of $Z^\star$, W is independent of $Z^\star$ as the shape of the filter is constant. Note further that a consequence of the ensemble average is that $\phi := |\Omega_i|/|\Omega| \equiv |W_i|/|W|$. Finally, we define a set of integers $A(Z^\star) \subset \{1, 2, \dots, N\}$ where $j \in A(Z^\star)$ if and only if the plane determined by $Z = Z^\star$ intersects $\partial\Omega_p^j$.

Given any function $\triangle = \triangle(\boldsymbol{X}, t)$ defined on Ω we define the cross-sectional average via

$$\bar{\triangle}(Z,t) := \frac{1}{\phi|W|}\int_{W_i} \triangle(\boldsymbol{X},t)\,\mathrm{d}S_X + \frac{1}{(1-\phi)|W|}\int_{W_p} \triangle(\boldsymbol{X},t)\,\mathrm{d}S_X, \quad Z \in (0,L), \tag{10}$$

where $\mathrm{d}S_X$ is a cross-sectional area element, with respect to $\boldsymbol{X}$. In particular, recall that $c \equiv 0$ for $\boldsymbol{X} \in \Omega_p$ so that

$$\bar{c}(Z,t) = \frac{1}{\phi|W|}\int_{W_i} c(\boldsymbol{X},t)\,\mathrm{d}S_X\,, \quad Z \in (0,L)\,. \tag{11a}$$

Application of Equation (10) to c_p, defined in Equation (9), yields

$$\bar{c}_p(Z,t) = \frac{1}{(1-\phi)|W|}\int_{W_p} c_p\,\mathrm{d}S_X = \frac{1}{(1-\phi)|W|}\sum_{j\in A(Z)}\int_{W_p^j} \langle c_p^j\rangle \mathrm{d}S_X\,, \quad Z \in (0,L)\,. \tag{11b}$$

Similarly, we calculate the cross-sectional average mass flux between the inter- and intra-particle regions given by

$$\bar{F}(Z,t) = \frac{1}{(1-\phi)|W|}\int_{W_p} F\,\mathrm{d}S_X\,, \quad Z \in (0,L)\,. \tag{11c}$$

Note that $\bar{c}(Z,t)$, $\bar{c}_p(Z,t)$ and $\bar{F}(Z,t)$, are now independent of X, Y and j.

At the fluid-fluid boundary we prescribe F on $\partial\omega$ combining a mass balance and a Newton cooling law:

$$F := \int_{\partial\omega} k_p(\bar{c} - \bar{c}_p)\,\mathrm{d}S_x \equiv |\partial\omega| k_p(\bar{c} - \bar{c}_p)\,, \tag{11d}$$

where we have introduced the proportionality constant k_p and the last equality follows from the fact that $\bar{c}$ and $\bar{c}_p$ are independent of $\boldsymbol{x}$, by construction. Thus, Equation (11c) simply yields

$$\bar{F} \equiv F\,. \tag{11e}$$

So that conservation of mass requires

$$\int_{\partial W_p} \left(\mathfrak{D}^{X,Y}\cdot\nabla_{\boldsymbol{X}}^{X,Y} c\right)\cdot \boldsymbol{n}_p^{X,Y}\,\mathrm{d}s_X = \frac{|W|(1-\phi)}{|\omega|}\bar{F}, \tag{12}$$

where $\boldsymbol{n}_p^{X,Y}$ is the normal to W_p, $\nabla_{\boldsymbol{X}}^{X,Y} := \left(\frac{\partial}{\partial X}, \frac{\partial}{\partial Y}\right)^\intercal$ and $\mathrm{d}s_X$ is the scalar line element with respect to $\boldsymbol{X}$.

2.2.1. Inter-particle

Taking the cross-sectional average (10) of Equation (2a) yields

$$\frac{\partial \bar{c}}{\partial t} + \upsilon \frac{\partial \bar{c}}{\partial Z} = \frac{1}{\phi |W|} \int_{W_i} \left(\nabla_{\boldsymbol{X}}^{X,Y} \cdot \left(\mathfrak{D}^{X,Y} \cdot \nabla_{\boldsymbol{X}}^{X,Y} c \right) + \frac{\partial}{\partial Z} \left(D \frac{\partial c}{\partial Z} \right) \right) \mathrm{d}S_X, \quad Z \in (0, L), \tag{13a}$$

where the left-hand side is a consequence of our assumption that changes to the volume and porosity of the solid structure are negligible and where we have decomposed the diffusive flux into the in plane and out of plane components. Noting $\partial W_i \equiv \partial W \cup \left(-\partial W_p\right)$, where the minus sign is used to preserve orientation, application of the Divergence theorem on Equation (13a) gives

$$\frac{\partial \bar{c}}{\partial t} + \upsilon \frac{\partial \bar{c}}{\partial Z} - D \frac{\partial^2 \bar{c}}{\partial Z^2} = \frac{1}{\phi |W|} \left[\int_{\partial W} \left(\mathfrak{D}^{X,Y} \cdot \nabla_{\boldsymbol{X}}^{X,Y} c \right) \cdot \boldsymbol{n}_o^{X,Y} \mathrm{d}s_X - \int_{\partial W_p} \left(\mathfrak{D}^{X,Y} \cdot \nabla_{\boldsymbol{X}}^{X,Y} c \right) \cdot \boldsymbol{n}_p^{X,Y} \mathrm{d}s_X \right], \quad Z \in (0, L), \tag{13b}$$

where we have once again used our assumption that changes to the volume and porosity of the solid structure are negligible and where $\boldsymbol{n}_o^{X,Y}$ is the in plane normal to the outer edge of the cylinder. As we assume that the filter is a cylinder of arbitrary cross-sectional shape, we have that the condition (2c) is equivalent to

$$\left(\mathfrak{D}^{X,Y} \cdot \nabla_{\boldsymbol{X}}^{X,Y} c \right) \cdot \boldsymbol{n}_o^{X,Y} = 0 \quad \boldsymbol{X} \in \partial W. \tag{14}$$

Thus, applying (14) and (12) to Equation (13b) yields the cross-sectionally averaged equation for the inter-particle concentration

$$\frac{\partial \bar{c}}{\partial t} + \upsilon \frac{\partial \bar{c}}{\partial Z} - D \frac{\partial^2 \bar{c}}{\partial Z^2} = -\frac{k_p (1-\phi)}{\phi} \frac{|\partial \omega|}{|\omega|} \left(\bar{c} - \bar{c}_p \right), \quad Z \in (0, L), \tag{15}$$

where the quantity $|\partial\omega|/|\omega|$ is known as the specific surface; in the case of spherical grains this is three times the inverse of the radius of the sphere.

2.2.2. Intra-particle

Currently, the governing equations for $\langle c_p^j \rangle$ and M_p^j are given in Equations (7) and (4), respectively, for a single arbitrary grain, the location of which depends on $\boldsymbol{X}$; now we take a cross-sectional average of these equations to determine their behaviour uniformly over the desired one-dimensional domain $Z \in \Omega$ — that is, $Z \in [0, L]$. Firstly, we define $\bar{m}_p$ with units moles/kg, to be the amount of adsorbate per unit mass of adsorbent,

$$\bar{m}_p(Z) := \frac{(1-\phi)\bar{m}_p}{\rho_b |\omega|} \equiv \frac{1}{\rho_b |W| |\omega|} \sum_{j \in A(Z)} \int_{W_p^j} M_p^j(\boldsymbol{X}, t) \mathrm{d}S_X, \tag{16}$$

where ρ_b is the bulk density and is defined to be the initial mass of the adsorbent divided by the total volume of the filter. We choose these units for $\bar{m}_p$ since this is a standard quantity use in experimental papers, *e.g.,* [4,14–16]. Consider

$$\begin{aligned} \frac{\partial \bar{c}_p}{\partial t} &= \frac{1}{(1-\phi)|W|} \sum_{j \in A(Z)} \int_{W_p^j} \frac{\partial \langle c_p^j \rangle}{\partial t} \, \mathrm{d}S_X \\ &= \frac{1}{(1-\phi)|W|} \sum_{j \in A(Z)} \int_{W_p^j} \left(-\frac{1}{\phi_p |\omega|} \frac{\partial M_p^j}{\partial t} + \frac{F_j}{\phi_p |\omega|} \right) \mathrm{d}S_X \\ &= -\frac{\rho_b}{\phi_p (1-\phi)} \frac{\partial \bar{m}_p}{\partial t} + \frac{k_p}{\phi_p} \frac{|\partial \omega|}{|\omega|} \left(\bar{c} - \bar{c}_p \right) \quad \text{for} \quad Z \in (0, L), \end{aligned} \tag{17}$$

where we have used Equation (7), the definitions (11b) and (16) of $\bar{c}_p$ and $\bar{m}_p$, $\bar{F}$ as defined in Equations (11c)–(11e) and the fact that $|\partial\omega|$, $|\omega|$, ϕ, ϕ_p are constant.

Now, we fix the macroscale function which describes the removal; we use the Sips model (see [10]) given by

$$\frac{\partial \bar{m}_p}{\partial t} = k_+ \bar{c}_p^a (\bar{m}_{\max} - \bar{m}_p)^b - k_- \bar{m}_p^b, \quad Z \in (0, L), \tag{18}$$

where a and b are integer exponents, k_+ and k_-, are the adsorption and desorption rate constants, respectively, and $\bar{m}_{\max}$ is the maximum amount of adsorbate that can attach to the adsorbent surface per mass of adsorbent. As is standard in literature surrounding chemistry and chemical engineering, the units of k_+ and k_- are not the same. Note that, when $a = b = 1$ Equation (18) reduces to the classical Langmuir-removal model.

At equilibrium, the concentration $\bar{c}$ is the same as the feed (or inlet) concentration, and the adsorbed amount, denoted $\bar{m}_e$ is

$$\bar{m}_e := \frac{\bar{m}_{max}}{1 + \left(\mathcal{K} c_{in}^a \right)^{-1/b}}, \tag{19}$$

where $\mathcal{K} := k_+/k_-$ is known as the equilibrium constant. Equation (19) this is known as the Sips isotherm.

2.3. Boundary conditions

We take the standard boundary and initial conditions [4–7,13]; conservation of flux at the inlet (Dankwert's condition), a passive outflow condition at the outlet, and initial conditions that the material is contaminant free:

$$v\bar{c}(0,t) - D\left.\frac{\partial \bar{c}}{\partial Z}\right|_{Z=0} = vc_{in}, \quad \text{for all } t, \tag{20a}$$

$$\left.\frac{\partial \bar{c}}{\partial Z}\right|_{Z=L} = 0, \quad \text{for all } t, \tag{20b}$$

$$\bar{c} = \bar{c}_p = \bar{m}_p = 0, \quad \text{at } t = 0. \tag{20c}$$

The asymmetry between the inlet and outlet conditions is explored and justified in Pearson [17].

2.4. Non-dimensionalisation

Our system is modelled by the coupled system of partial differential equations formed by Equations (15), (17), and (18), and subject to the boundary conditions (20). We non-dimensionalise via the scalings

$$\bar{c} = c_{in}C, \quad \bar{c}_p = c_{in}C_p, \quad \bar{m}_p = \bar{m}_e m_p, \quad Z = \mathcal{L}\zeta, \quad \text{and} \quad t = \mathcal{T}\tau, \tag{21a}$$

where c_{in} is the inlet concentration, $\bar{m}_e$ is defined in Equation (19), $\mathcal{L}$ is the reaction length scale and $\mathcal{T}$ is the reactive timescale. The reaction length scale is obtained via balancing advection with the rate of removal ($\partial m_p/\partial t$) in Equations (15) and (17) and the reactive timescale is obtained via balancing the rate of removal with adsorption in Equation (18) giving

$$\mathcal{L} := \frac{v\mathcal{T}\phi c_{in}}{\rho_b \bar{m}_e} \quad \text{with} \quad \mathcal{T} := \frac{\bar{m}_e^{1-b}}{k_+ c_{in}^a}. \tag{21b}$$

We denote the dimensionless length of the filter as $l := L/\mathcal{L}$. Employing the scaling (21) on Equations (15), (17), (18), and the boundary conditions (20) yields

$$\mathrm{Da}\frac{\partial C}{\partial \tau} + \frac{\partial C}{\partial \zeta} - \mathrm{Pe}^{-1}\frac{\partial^2 C}{\partial \zeta^2} = -\left(\alpha\frac{\partial C_p}{\partial \tau} + \frac{\partial m_p}{\partial \tau}\right), \tag{22a}$$

$$\alpha\frac{\partial C_p}{\partial \tau} + \frac{\partial m_p}{\partial \tau} = \beta\left(C - C_p\right), \tag{22b}$$

$$\frac{\partial m_p}{\partial \tau} = C_p^a\left(\mu - m_p\right)^b - (\mu - 1)^b m_p^b, \tag{22c}$$

subject to

$$C(0,\tau) - \mathrm{Pe}^{-1}\left.\frac{\partial C}{\partial \zeta}\right|_{\zeta=0} = 1, \quad \text{for all} \quad \tau > 0, \tag{23a}$$

$$\left.\frac{\partial C}{\partial \zeta}\right|_{\zeta=l} = 0, \quad \text{for all} \quad \tau > 0, \tag{23b}$$

$$C(\zeta,0) = C_p(\zeta,0) = m_p(\zeta,0) = 0, \quad \text{for all} \quad \zeta \in (0,l), \tag{23c}$$

where we have defined

$$\begin{aligned} &\mathrm{Da} := \frac{\mathcal{L}}{v\mathcal{T}}, \quad \mathrm{Pe} := \frac{v\mathcal{L}}{D}, \quad \mu := \frac{\bar{m}_{\max}}{\bar{m}_e} = 1 + \left(\mathcal{K}c_{in}^a\right)^{-1/b}, \\ &\alpha := \frac{\phi_p \mathrm{Da}}{\varphi}, \quad \beta := k_p\frac{|\partial\omega|}{|\omega|}\frac{\mathcal{T}\mathrm{Da}}{\varphi}, \quad \text{with} \quad \varphi := \frac{\phi}{1-\phi}. \end{aligned} \tag{24}$$

The parameters Da and Pe are the Damköhler and Péclet numbers, respectively.

2.5. Parameter values

The specific surface, $|\partial\omega|/|\omega|$, is the ratio of grain surface area to volume and satisfies that $|\partial\omega|/|\omega| \geq 3/R$, where we define R to equal the shortest distance from the centre of a grain to the point on the surface that is furthest away from the centre (*e.g.,* R is the distance from the centre of a cube to one of the vertices). Note that this ratio is minimised for a sphere (see [18]).

The coefficient of the rate of change of concentration within each porous grain, α, can be thought of as the ratio of the flow timescale to the reaction timescale within each porous grain, that is, an 'internal' Damköhler number. Provided the porous grains of adsorbent have a non-negligible fluid-fraction (*i.e.,* $\phi_p \ll 1$) and that the column is neither too packed ($1 - \phi \ll 1$) nor too empty

($\phi \ll 1$), then $\alpha = \mathcal{O}(\mathrm{Da})$. Alternatively, using the definition of $\mathcal{L}$ and Da, $\alpha \equiv \phi_p(1-\phi)c_{in}/(\rho_b \bar{m}_e)$ is the ratio of the maximum amount of contaminant that can occupy all porous particles to the amount that the porous particles can adsorb per unit length.

Adsorption columns work by forcing a contaminated fluid through a column packed with an adsorbent material. In this situation it is well-known that advection dominates over diffusion/dispersion resulting in a large value of the Péclet number, *i.e.*, $\mathrm{Pe}^{-1} \ll 1$. The Damköhler number Da corresponds to the ratio of the flow time-scale to the adsorption time-scale. The fluid takes of the order of seconds to pass through a column, while the adsorption process often lasts for hours, consequently $\mathrm{Da} \ll 1$. Finally, α is proportional to Da so will also be small. Experimental data (*e.g.,* [4–7,13,19–21]) suggests the following ranges for parameters: $\phi_p, \phi \in (0.2, 0.8)$ which gives $\varphi \in (1/4, 4) = \mathcal{O}(1)$; $\mathrm{Pe}^{-1} \in (10^{-4}, 10^{-1})$; and $\alpha \sim \mathrm{Da} \in (10^{-6}, 10^{-3})$. In practical situations, adsorption should dominate over desorption thus, in general we expect $\mathcal{K} = k_+/k_- \gg 1$. Since $\mu = 1 + 1/(\mathcal{K}c_{in}^a)^{1/b}$, this suggests $\mu = \mathcal{O}(1)$ (with $\mu > 1$).

The parameter β results from scaling the Newton Cooling condition (11d) with the removal inside porous grains. It can be thought of as the ratio of the macroscale reactive timescale $\mathcal{T}$ over the timescale

$$\mathcal{T}_\beta := \frac{\rho_b \bar{m}_e |\omega|}{c_{in} k_p (1-\phi)\,|\partial\omega|}, \tag{25}$$

associated with the entry of the contaminant into a porous grain and its subsequent removal via adsorption. In what follows, we analyse the effects of varying β on the effective performance of the filter.

$\beta \gg 1$: in this regime contaminant almost instantly diffuses into the particle once it reaches the porous grain. In this case it is possible to use effective parameters to obtain a governing set of equations that are structurally identical to the classical models. This allows the whole dual porosity medium to be described by an equivalent single porosity medium with an effective porosity at leading order:

$$\check{\mathrm{Da}}\frac{\partial C}{\partial \tau} + \frac{\partial C}{\partial \zeta} - \mathrm{Pe}^{-1}\frac{\partial^2 C}{\partial \zeta^2} = -\frac{\partial m_p}{\partial \tau}, \tag{26a}$$

$$\frac{\partial m_p}{\partial \tau} = C^a\left(\mu - m_p\right)^b - (\mu-1)^b (m_p)^b, \tag{26b}$$

where $\check{\mathrm{Da}} := \alpha + \mathrm{Da}$. Thus, in this limit we replace the 'inter-particle' porosity ϕ with an effective porosity $\check{\phi}$ given by $\check{\phi} := \phi(1-\phi_p) + \phi_p$. Note that, $\check{\phi} \le 1$ because $(1-\phi_p) + \phi_p = 1$ and $\phi \le 1$. This is often referred to as a model with reservoir effects [22]. To reproduce the classical model (with $\Phi = \phi$) we take the limit of impermeable grains; thus, $\phi_p \to 0 \implies \alpha \to 0$ so that $\check{\mathrm{Da}} \to \mathrm{Da}$. This limiting process corresponds to converting the total adsorption internally within each grain to an effective removal on the surface of the porous grains.

$\beta \sim 1$: In this regime the diffusion within the porous grain balances the rate at which contaminant advects to the surface of the porous grain in the interparticle domain. In this dual porosity limit the interplay between the inter- and intra-particle regions is crucial.

$\beta \ll 1$: In this regime we have a very ineffective filter. At leading order we reproduce the single porosity limit [22] but with no removal

$$\mathrm{Da}\frac{\partial C}{\partial \tau} + \frac{\partial C}{\partial \zeta} - \mathrm{Pe}^{-1}\frac{\partial^2 C}{\partial \zeta^2} = 0. \tag{27}$$

This essentially corresponds to when the time taken to diffuse contaminant within the porous particles is much slower than the rate at which contaminant is advected to the porous grains. We also note that β strongly depends on the porosity of the bulk material and on the specific surface of the grains. In particular, a large porosity (φ large) and a small specific surface produce a small value of β.

Given that the limit $\beta \ll 1$ reduces to the classical model, and $\beta \gg 1$ corresponds to negligible removal, in what follows we focus on the limit $\beta \sim 1$.

3. Solution methods

3.1. Numerical solution of the full system of partial differential equations

In general, we solve the initial-boundary value problem (IBVP) (22), (23) numerically. We tackle this IBVP via a combination of the method of lines and Chebyshev spectral collocation (*i.e.*, Chebyshev pseudospectral methods) [23–26]. That is, we discretise the spatial domain into the N Chebyshev points and then approximate spatial derivatives using a dense Chebyshev differentiation matrix [27]; this approach allows for simple incorporation of the boundary conditions into the Chebyshev pseudospectral differentiation matrix. We subsequently integrate the resulting system of differential algebraic equations (DAEs) in time with MATLAB® using `ode15s` [26,28]. The Chebyshev pseudospectral method has proved to be more robust than classical finite volumes or finite differences; this is because a change at any collocation point affects every other collocation point, while a change in a simple finite differences discretisation will only affect its neighbours. More detail on this approach is given in Appendix A. As we will discuss in §3.4, due to the form of the full numerical solution, we make a travelling wave assumption to reduce the problem to a system of first

order ODEs with a boundary condition and an internal constraint for which we also solve via Chebyshev spectral collocation (see §3.4.2).

3.2. Steady-state solutions

At steady state, the system (22) becomes

$$\frac{\partial C}{\partial \zeta} - \mathrm{Pe}^{-1}\frac{\partial^2 C}{\partial \zeta^2} = 0, \tag{28a}$$

$$C = C_p, \tag{28b}$$

$$\left(C_p\right)^a(\mu - m_p)^b - (\mu - 1)^b (m_p)^b = 0, \tag{28c}$$

subject to the boundary conditions (23a,b). Hence the steady state solution is simply

$$C(\zeta,\tau) = C_p(\zeta,\tau) = m_p(\zeta,\tau) \equiv 1. \tag{29}$$

This trivial solution will be used in §3.4 as a boundary condition for a travelling wave approximation.

3.3. Early time solution

Here, we investigate the form of the solutions at early times. Early time solutions are often useful to determine a starting point for a numerical scheme, particularly when the exact initial condition is discontinuous. Our simulations do not suffer from this problem, instead we use the early time solution to verify the numerical solution close to the initial condition.

We take $T = \tau/\delta$ and note that for small time we expect $\mathcal{O}(1)$ changes in C and C_p but only $\mathcal{O}(\delta)$ changes in m_p. That is, in a small time, we expect the filter to use up only a small fraction of its available adsorption sites which implies that m_p scales like $\delta\mathcal{M}$. Thus, we take $\mathcal{M} = m_p/\delta$ and the system (22) becomes

$$\frac{\mathrm{Da}}{\delta}\frac{\partial C}{\partial T} + \frac{\partial C}{\partial \zeta} - \mathrm{Pe}^{-1}\frac{\partial^2 C}{\partial \zeta^2} = -\left(\frac{\partial \mathcal{M}}{\partial T} + \frac{\alpha}{\delta}\frac{\partial C_p}{\partial T}\right), \tag{30a}$$

$$\frac{\alpha}{\delta}\frac{\partial C_p}{\partial T} + \frac{\partial \mathcal{M}}{\partial T} = \beta\left(C - C_p\right), \tag{30b}$$

$$\frac{\partial \mathcal{M}}{\partial T} = \left(C_p\right)^a(\mu - \delta\mathcal{M})^b - (\mu - 1)^b(\delta\mathcal{M})^b, \tag{30c}$$

subject to the boundary and initial conditions (23). Then, for any δ satisfying $\mathrm{Da} \ll \delta \ll 1$ and $\mathrm{Pe} \ll 1$ the leading order terms ($C^{(0)}$, $\mathcal{M}^{(0)}$ and $C_p^{(0)}$) are found to satisfy

$$\frac{\partial C^{(0)}}{\partial \zeta} = -\frac{\partial \mathcal{M}^{(0)}}{\partial T}, \tag{31a}$$

$$\frac{\partial \mathcal{M}^{(0)}}{\partial T} = \beta\left(C^{(0)} - C_p^{(0)}\right), \tag{31b}$$

$$\frac{\partial \mathcal{M}^{(0)}}{\partial T} = \mu^b\left(C_p^{(0)}\right)^a, \tag{31c}$$

subject to

$$\text{(i)}\quad C^{(0)}(0,T) = 1, \quad \text{and} \quad \text{(ii)}\quad \left.\frac{\partial C^{(0)}}{\partial \zeta}\right|_{\zeta = l} = 0. \tag{32}$$

Rearranging the early-time system (31) gives

$$\frac{\partial C_p^{(0)}}{\partial \zeta}\left(1 + \frac{\mu^b}{\beta}a(C_p^{(0)})^{a-1}\right) = -C_p^{(0)}\mu^b, \tag{33a}$$

$$C^{(0)} = \left(1 + \frac{\mu^b}{\beta}\right)C_p^{(0)}, \tag{33b}$$

$$\frac{\partial \mathcal{M}^{(0)}}{\partial T} = (C_p^{(0)})^a\mu^b. \tag{33c}$$

Equation (33a) can be solved explicitly, which determines $C_p^{(0)}$ and $C^{(0)}$ via Equation (33b).

For the case where $a = 1$, the general solution to the problem (32), (33) is

$$C_p^{(0)}(\zeta,T) = \varphi(T)e^{-\beta\mu^b\zeta/(\beta+\mu^b)}, \qquad C^{(0)} = \frac{\beta+\mu^b}{\beta}\varphi(T)e^{-\beta\mu^b\zeta/(\beta+\mu^b)}. \tag{34}$$

Note that there is only one free parameter, the time-dependent function $\varphi(T)$, however, $C(\zeta,T)$ is subject to the two boundary conditions (32). Thus, it is not possible to find a function $C(\zeta,T)$ that satisfies both boundary conditions; it is natural to choose the inlet condition (32.i) since the process is driven by the input at $\zeta=0$. Further, imposing the boundary condition (32.ii) would yield the trivial solution $C^{(0)}=C_p^{(0)}=\mathcal{M}^{(0)}\equiv 0$. Therefore, the solution of Equation (31) subject to (32.i) gives

$$C_p^{(0)}=\frac{\beta}{\beta+\mu^b}e^{-\beta\mu^b\zeta/(\beta+\mu^b)},\quad C^{(0)}=e^{-\beta\mu^b\zeta/(\beta+\mu^b)},\quad \mathcal{M}^{(0)}=\frac{\beta T}{\beta+\mu^b}e^{-\beta\mu^b\zeta/(\beta+\mu^b)}. \tag{35}$$

We note that,

$$\lim_{\zeta\to\infty}C^{(0)}=\lim_{\zeta\to\infty}\frac{\partial C^{(0)}}{\partial\zeta}=0. \tag{36}$$

Therefore, in an infinite filter the boundary condition at the outlet would also be satisfied. Further, Equation (33a) shows that for any value of $a\geq 1$ smooth solutions satisfy conditions (36). In a filter of finite length the boundary condition at the outlet is satisfied by means of a trivial boundary layer (that is $C^{(0)}$ =constant) of length δ.

3.4. Travelling wave approximation

The numerical solution to the IBVP (22), (23) implies that for certain parameter regimes and sufficiently large time, C, C_p and m_p behave like travelling waves (see Figs. 3 and 4, and related discussion in §3.5). Thus, we introduce a travelling wave coordinate

$$\eta:=\zeta-S(\tau). \tag{37}$$

We fix the location of the wavefront via

$$S(\tau)=\dot{S}(\tau-\tau_{1/2})+l, \tag{38}$$

where the wave velocity $\dot{S}:=\mathrm{d}S/\mathrm{d}\tau$ is a constant to be determined during the solution process and $\tau_{1/2}$ is the (dimensionless) time at which the concentration at the outlet is exactly half that at the inlet (termed the half-time), that is,

$$C(l,\tau_{1/2})=\frac{1}{2}. \tag{39}$$

We define

$$C(\zeta,\tau):=C(\eta),\quad C_p(\zeta,\tau):=C_p(\eta),\quad \text{and}\quad m_p(\zeta,\tau):=\mathcal{M}_p(\eta), \tag{40}$$

so that the system (22) becomes

$$\left(1-\mathrm{Da}\,\dot{S}\right)\frac{\mathrm{d}C}{\mathrm{d}\eta}=\mathrm{Pe}^{-1}\frac{\mathrm{d}^2C}{\mathrm{d}\eta^2}+\alpha\dot{S}\frac{\mathrm{d}C_p}{\mathrm{d}\eta}+\dot{S}\frac{\mathrm{d}\mathcal{M}_p}{\mathrm{d}\eta}, \tag{41a}$$

$$\beta\left(C-C_p\right)=-\dot{S}\left(\alpha\frac{\mathrm{d}C_p}{\mathrm{d}\eta}+\frac{\mathrm{d}\mathcal{M}_p}{\mathrm{d}\eta}\right), \tag{41b}$$

$$-\dot{S}\frac{\mathrm{d}\mathcal{M}_p}{\mathrm{d}\eta}=C_p^a\left(\mu-\mathcal{M}_p\right)^b-(\mu-1)^b\mathcal{M}_p^b, \tag{41c}$$

and where the condition (39) fixes

$$C(0)=1/2. \tag{42}$$

For the travelling wave approximation we need to consider filters of an infinite length. We thus need to impose boundary conditions at plus and minus infinity. Due to the transformation (37), the limit $\eta\to-\infty$ corresponds to $\tau\to+\infty$ hence the steady state solution (29) holds and we impose

$$\lim_{\eta\to-\infty}C=\lim_{\eta\to-\infty}C_p=\lim_{\eta\to-\infty}\mathcal{M}_p=1,\quad \lim_{\eta\to-\infty}\frac{\mathrm{d}C}{\mathrm{d}\eta}=0. \tag{43a}$$

These conditions are a natural choice since they correspond to a steady flow of pollutant sufficiently far upstream and that the filter is fully saturated there. As $\eta\to\infty$ one expects the fluid to be clean and the filter fresh, thus we impose

$$\lim_{\eta\to\infty}C=\lim_{\eta\to\infty}C_p=\lim_{\eta\to\infty}\mathcal{M}_p=\lim_{\eta\to\infty}\frac{\mathrm{d}C}{\mathrm{d}\eta}=0. \tag{43b}$$

By integrating Equation (41a) and imposing the conditions (43b) in the limit $\eta\to\infty$, we find

$$\left(1-\mathrm{Da}\,\dot{S}\right)C=\mathrm{Pe}^{-1}\frac{\mathrm{d}C}{\mathrm{d}\eta}+\dot{S}(\alpha C_p+\mathcal{M}_p). \tag{44a}$$

Imposition of the conditions (43a) determines the wave velocity $\dot{S}$:

$$\dot{S} = \frac{1}{1+\alpha+\mathrm{Da}}. \tag{44b}$$

In general, we solve Equations (41b), (41c), (44a) numerically, assuming that $\eta \in [-B, B]$, where B is some large number, subject to $\mathcal{M}_p(B) = 0$. Details of the numerical scheme are given in §3.4.2 and the associated MATLAB codes have been uploaded to Github (https://github.com/aguareles/Intra-particle-diffusion.git). However, by taking advantage of the small parameters in the system, for certain combinations of a and b, we are able to determine approximate analytical solutions. Recall that for the physically relevant parameter regimes of the present study $\alpha, \mathrm{Da}, \mathrm{Pe}^{-1} \ll 1$. Neglecting these terms, Equation (44b) simply becomes $\dot{S} = 1$, while Equation (44a) yields $C = \mathcal{M}_p$. Equation (41b) reduces to a first order ordinary differential equation for $C(\eta)$ with C_p determined implicitly via Equation (41c)

$$\frac{\mathrm{d}C}{\mathrm{d}\eta} = -\beta\left(C - C_p\right), \tag{45a}$$

$$\beta\left(C - C_p\right) = C_p^a(\mu - C)^b - (\mu-1)^b C^b. \tag{45b}$$

The following proposition establishes the conditions under which the system (45) provides a unique solution satisfying (42) and (43), that is

$$C(0) = 1/2, \quad \lim_{\eta\to-\infty} C = 1, \quad \lim_{\eta\to\infty} C = 0. \tag{46}$$

Proposition 1. *Given $\mu, \beta, c_0 \in \mathbb{R}$ such that $\mu > 1$, $\beta > 0$, and $0 < c_0 < 1$, for any $a, b \in \mathbb{N}$ such that $a \le b$, the initial value problem given by Equation (45a) and the initial condition*

$$C(0) = c_0 \in (0,1), \tag{47}$$

where $C_p(C)$ is implicitly determined by (45b) is well posed and it has a unique decreasing solution, $C(\eta)$ satisfying the conditions at plus and minus infinity provided in (46).

The proof of this proposition is provided in Appendix B.

Proposition 1 states the existence of travelling waves as solutions of the reduced system (45) when $a \le b$, but further analysis is needed to study cases where $a > b$. However, $a \le b$ is the physically relevant case in adsorption settings. The physical reaction associated with an (a, b) integer pair is

$$a\mathcal{A} + b\mathcal{B} \underset{k_-}{\overset{k_+}{\rightleftharpoons}} \text{Adsorbate}, \tag{48}$$

where $\mathcal{A}$ and $\mathcal{B}$ refer to the pollutant molecules and adsorbent sites, respectively. Although the case $a > b$ may appear an advantageous situation (each adsorbent site $\mathcal{B}$ is capable of capturing a/b pollutant molecules $\mathcal{A}$), the equilibrium of this reaction provides a very slow increase of the adsorbed fraction at equilibrium $\bar{m}_e$ with respect to the inlet concentration. Thus, even high concentrations result in a scarce adsorption capacity. The cases in which $a > b$, provide convex isotherms that are regarded as unfavourable adsorption cases [29].

In what follows we restrict ourselves to $a \le b$. Analytical solutions can be determined for certain values of a and b. When such solutions can be found, they may be determined via separation of variables in Equation (45a), which yields

$$-\beta\eta = \int_{1/2}^{C} \frac{\mathrm{d}u}{u - C_p(u)} = \int_{1/2}^{C} f(u)\mathrm{d}u = F(C) - F(1/2), \tag{49}$$

where F is defined by

$$F(C) = \int_0^C f(u)\mathrm{d}u, \tag{50}$$

and depends on the Sips exponents, a and b. In what follows we consider some specific combinations of (a, b) that are commonly found in the adsorption literature [13].

3.4.1. Explicit solutions for typical parameter values

When $a = 1$, Equation (45b) can be rearranged as follows

$$C_p = \frac{(\mu-1)^b C^b + \beta C}{\beta + (\mu - C)^b}, \tag{51}$$

which we use to write Equation (45a) as

$$\frac{\mathrm{d}C}{\mathrm{d}\eta} = -\beta\frac{C(\mu-C)^b - (\mu-1)^b C^b}{\beta + (\mu-C)^b}, \tag{52}$$

Table 1
Summary of expressions for $F(C)$ defined in Equation (50), for different values of a, b.

$a=1$	$F(C)$
$b=1$	$(\beta+\mu)\ln(C)+(1-\beta-\mu)\ln(1-C)$
$b=2$	$\left(\frac{\beta}{\mu^2}+1\right)\ln(C)-\frac{\beta+(\mu-1)^2}{\mu^2-1}\ln(1-C)+\frac{\beta+\mu^2(\mu-1)^2}{\mu^2(\mu^2-1)}\ln(\mu^2-C)$
$b=3,\ \mu\in(1,4)$	$\left(\frac{\beta}{\mu^3}+1\right)\ln(C)-A_1\ln(1-C)+A_2\ln\left[(C-q_1)^2+q_2^2\right]-\frac{A_3}{q_2}\arctan\left(\frac{C-q_1}{q_2}\right)$ where, q_1 and q_2 are defined in Equation (56) and where $A_1:=\frac{\beta+(\mu-1)^3}{(\mu-1)^2(2\mu+1)}$, $A_2:=\frac{\mu^3(\mu-1)^3+\beta(2q_1-1)}{2\mu^3(\mu-1)^2(2\mu+1)}$ and $A_3:=\frac{\beta[3-\mu(4-\mu)(\mu-1)]+3(\mu-1)^3\mu^3}{2\mu(\mu-1)(2\mu+1)}$
$b=3,\ \mu=4$	$\frac{\beta+64}{64}\ln(C)-\frac{\beta+27}{81}\ln(1-C)+\frac{1728-17\beta}{5184}\ln(C+8)+\frac{\beta+1728}{72(C+8)}$
$b=3,\ \mu>4$	$\left(\frac{\beta}{\mu^3}+1\right)\ln(C)-A_1\ln(1-C)+\left[\frac{\beta+(\mu-n_+)^3}{n_+(1-n_+)(n_+-n_-)}\right]\ln(C-n_+)+\left[\frac{\beta+(\mu-n_-)^3}{n_-(1-n_-)(n_--n_+)}\right]\ln(C-n_-)$ where A_1 is defined above, in the case $b=3$, $\mu\in(1,4)$, and where $n_\pm$ are defined in Equation (58b).

with implicit solution

$$-\beta\eta=\int_{1/2}^{C}\frac{\beta+(\mu-u)^b}{u(\mu-u)^b-(\mu-1)^b u^b}\mathrm{d}u=F(C)-F(1/2)\,. \tag{53}$$

The evaluation of the integral when $b=1$ and $b=2$ is straightforward. When $b=3$, the form of the solution depends on the number of real roots of the polynomial in the denominator of Equation (53):

$$p(C):=C(\mu-C)^3-(\mu-1)^3C^3\,. \tag{54}$$

When $\mu\in(1,4)$, $p(C)$ has only two real roots ($C=0,1$), so we decompose it as follows

$$p(C)=C(1-C)((C-q_1)^2+q_2^2) \tag{55}$$

where

$$q_1:=\frac{\mu^2(3-\mu)}{2},\quad\text{and}\quad q_2^2:=\mu^3-\frac{\mu^4(3-\mu)^2}{4}\equiv\frac{\mu^3(4-\mu)(\mu-1)^2}{4}\,. \tag{56}$$

There exists a critical value of μ, ($\mu=4$), such that $p(C)$ has three real roots, one of which has a double multiplicity; in this case $p(C)$ can be expressed as

$$p(C)=C(1-C)(C+8)^2. \tag{57}$$

When $\mu>4$, $p(C)$ has four distinct real roots ($C=0,1$), so we decompose it as follows

$$p(C)=C(1-C)(C-n_+)(C-n_-)\,, \tag{58a}$$

with

$$n_\pm:=\frac{\mu^2(3-\mu)\pm\sqrt{\mu^4(3-\mu)^2-4\mu^3}}{2}. \tag{58b}$$

Table 1 summarises the expressions for $F(C)$ for the above combinations of a and b.

3.4.2. *Numerical solutions for travelling waves*

Equations (41b), (41c), and (44a) define a system of three coupled first order ODEs subject to one constraint on C at $\eta=0$ (equation (42)). To solve this numerically we must approximate the infinite domain with a large but finite domain; as such we take $\eta\in[-B,B]$, where B is a large constant. We choose B to be sufficiently large so that

$$\frac{\mathrm{d}C}{\mathrm{d}\eta},\ \frac{\mathrm{d}C_p}{\mathrm{d}\eta},\ \frac{\mathrm{d}\mathcal{M}_p}{\mathrm{d}\eta}\to 0\qquad\text{as}\qquad\eta\to\pm B, \tag{59}$$

i.e., the solution profiles tend to constant values at $\eta\to\pm B$. In particular, in Figs. 3 and 4 we take $B=80$. In addition to the specified equations and conditions we must also impose a further condition at $\eta=B$ to fix the wave position, in the code we choose to enforce $\mathcal{M}_p(B)=0$ (although we could equally well choose $C(B)=0$ or $C_p(0)$). To solve this numerically, we use a direct method based on Chebyshev spectral collocation; we discretise the spatial domain into an odd number of collocation points (to allow for easier enforcement of the condition at $\eta=0$) and use a dense Chebyshev differentiation matrix to discretise the derivatives and determine an objective function. We solve this nonlinear system via Newton iteration updating the solution via the analytically determined Jacobian (see Appendix A) and terminating once the objective function is sufficiently small.

3.4.3. Breakthrough curves

When Da and α are neglected, Equation (44b) reduces to $\dot{S} = 1$. Therefore, the solution for any a, b combination is given implicitly for $C(\zeta, \tau)$ by

$$-\beta\left[\zeta - l - \left(\tau - \tau_{1/2}\right)\right] = F(C) - F\left(\frac{1}{2}\right), \tag{60a}$$

for $m_p(Z,t)$ by

$$-\beta\left[\zeta - l - \left(\tau - \tau_{1/2}\right)\right] = F(m_p) - F\left(\frac{1}{2}\right) \tag{60b}$$

and implicitly for $C_p(\zeta,\tau)$ via substitution of $C(\zeta,\tau)$ in Equation (51). It is straightforward to find the breakthrough curves by evaluating Equation (60a) at $\zeta = l$. In particular, the breakthrough curves that correspond to the analytical solutions presented in Table 1, read:

- $a = 1, b = 1$:

$$-\beta(\tau - \tau_{1/2}) = (\beta + \mu)\ln(2C) + (1 - \beta - \mu)\ln(2(1 - C)), \tag{61}$$

- $a = 1, b = 2$:

$$-\beta(\tau - \tau_{1/2}) = \left(\frac{\beta}{\mu^2} + 1\right)\ln(2C) - \frac{\beta + (\mu-1)^2}{\mu^2 - 1}\ln(2(1-C)) + \frac{\beta + \mu^2(\mu-1)^2}{\mu^2(\mu^2-1)}\ln\left(\frac{\mu^2 - C}{\mu^2 - 1/2}\right) \tag{62}$$

- $a = 1, b = 3$:
  If $\mu \in (1,4)$:

$$\begin{aligned}-\beta(\tau - \tau_{1/2}) = &-\left(\frac{\beta}{\mu^3} + 1\right)\ln(2C) - A_1\ln(2(1-C)) + A_2\ln\left(\frac{(C-q_1)^2 + q_2^2}{(1/2-q_1)^2 + q_2^2}\right) \\ &- \frac{A_3}{q_2}\left(\arctan\left(\frac{C-q_1}{q_2}\right) + \arctan\left(\frac{1/2-q_1}{q_2}\right)\right),\end{aligned} \tag{63}$$

  where A_1, A_2, A_3, q_1, q_2, as defined in Table 1, are constants that depend on μ and β.
  If $\mu = 4$:

$$-\beta(\tau - \tau_{1/2}) = \left(\frac{\beta}{\mu^3} + 1\right)\ln(2C) - A_1\ln(2(1-C)) + \left(\frac{\beta + (\mu - n_+)^3}{n_+(1-n_+)(n_+ - n_-)}\right)\ln\left(\frac{C - n_+}{1/2 - n_+}\right). \tag{64}$$

  If $\mu > 4$,

$$-\beta(\tau - \tau_{1/2}) = \left(\frac{\beta}{\mu^3} + 1\right)\ln(2C) - A_1\ln(2(1-C)) + \left(\frac{\beta + (\mu - n_+)^3}{n_+(1-n_+)(n_+ - n_-)}\right)\ln\left(\frac{C - n_+}{1/2 - n_+}\right), \tag{65}$$

  where A_1 is defined in Table 1 and $n_\pm$ are defined in Equation (58b).

3.5. Comparison with numerical simulations

In Figs. 3 and 4 we compare the numerical solution of the full IBVP (22), (23), the numerical solution of the travelling wave approximation (41), and the analytical solution derived in §3.4.1 after setting $\alpha, \mathrm{Da}, \mathrm{Pe}^{-1} = 0$ in the system (41). The parameter values for Fig. 3 have been chosen to be representative of the experimental data in §4.1, while those for Fig. 4 are representative of the experimental data in §4.2.

The first row in both figures shows the evolution of the travelling wave along the adsorption column (blue to yellow as τ increases). We can see how the initial transient evolves until it matches the early-time solutions (shown as a dashed red line) discussed in §3.3. For larger times the system follows the travelling wave form. In Fig. 3, corresponding to Hg(II), the wave front becomes steeper with increasing b. In Fig. 4 the front is steepest for low b.

In the second row of both figures we show curves corresponding to constant $C(\zeta^*(\tau),\tau) = 0.1$, 0.5, and 0.9. If a travelling wave occurs we should observe that

$$\zeta^*(\tau) = \dot{S}\tau + \kappa. \tag{66}$$

Taking logarithms of both sides,

$$\log(\zeta^*) = \log(\dot{S}\tau + \kappa) = \log(\tau) + \log(\dot{S}) + \log\left(1 + \frac{\kappa}{\dot{S}\tau}\right). \tag{67}$$

For sufficiently large values of τ the final term is negligible and therefore, if there is a travelling wave, the three curves must become co-linear. In all cases they coincide for $\tau = \mathcal{O}(1)$, which is precisely the time regime when the travelling wave is formed after the

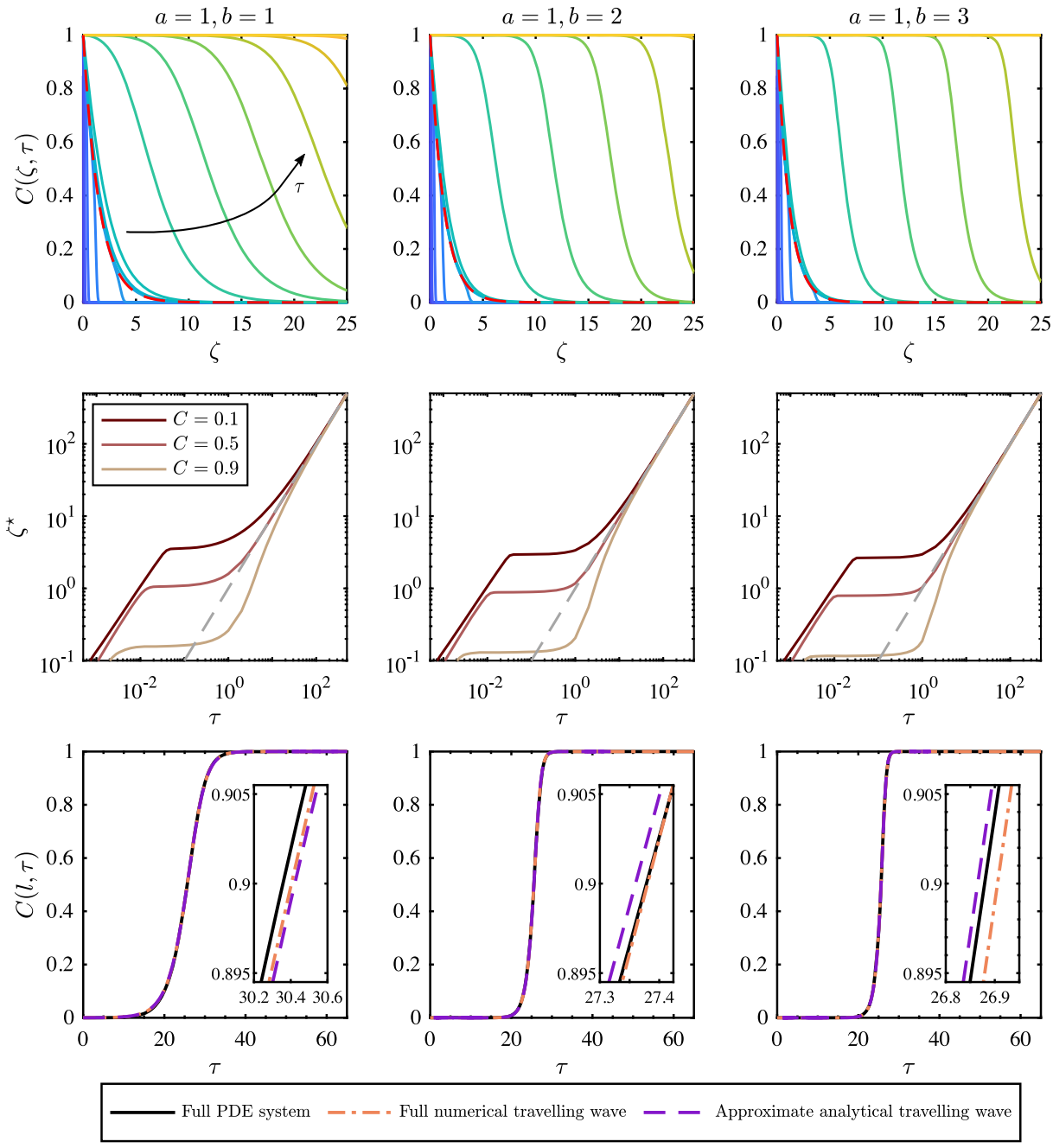

Fig. 3. ***First row***: evolution of the travelling wave with respect to time (blue to yellow) for different combinations of a, b. We take logarithmically spaced times for $\mathrm{Da}\,\mathrm{Pe}^{-1} \leq \tau \leq 1$ and linearly spaced values thereafter, $\tau \in \{5.0\times10^{-5}, 1.5\times10^{-4}, 4.5\times10^{-4}, 1.4\times10^{-3}, 4.1\times10^{-3}, 0.012, 0.037, 0.11, 0.33, 1, 6.6, 12, 18, 24, 29, 34, 40\}$. The early time solution of §3.3 (red dashed lines) shows the quasi-steady state of the solution profile for $\tau = O(\delta)$. ***Second row***: the three curves correspond to $C(\zeta^*(\tau), \tau) = 0.1, 0.5$ and 0.9 in logarithmic scale. ***Third row***: breakthrough curves obtained by numerically solving the system of partial differential equations (22), (23), the full travelling wave system (41) and the analytical solutions given in §3.4.1. The parameter values are: $l = 25$ (first and third rows) $l = 500$ (second row), $\mu = 1.9125$, $\mathrm{Pe}^{-1} = 5\times10^{-3}$, $\beta = 1$, $\mathrm{Da} = 2\alpha = 0.01$.

initial transient. In each case the slope corresponds to $\dot{S}$. Note that although this method does not represent a rigorous proof for the existence of travelling waves, it is very useful in suggesting when they will exist. The plots in Figs. 3 and 4 are consistent with the conjecture presented in §3.4 on the existence of travelling waves.

The third row shows the breakthrough curves obtained by numerically solving the system of partial differential equations (22), (23), the full travelling wave system (41), and the analytical solutions given in §3.4.1. The figures show that there is a very good

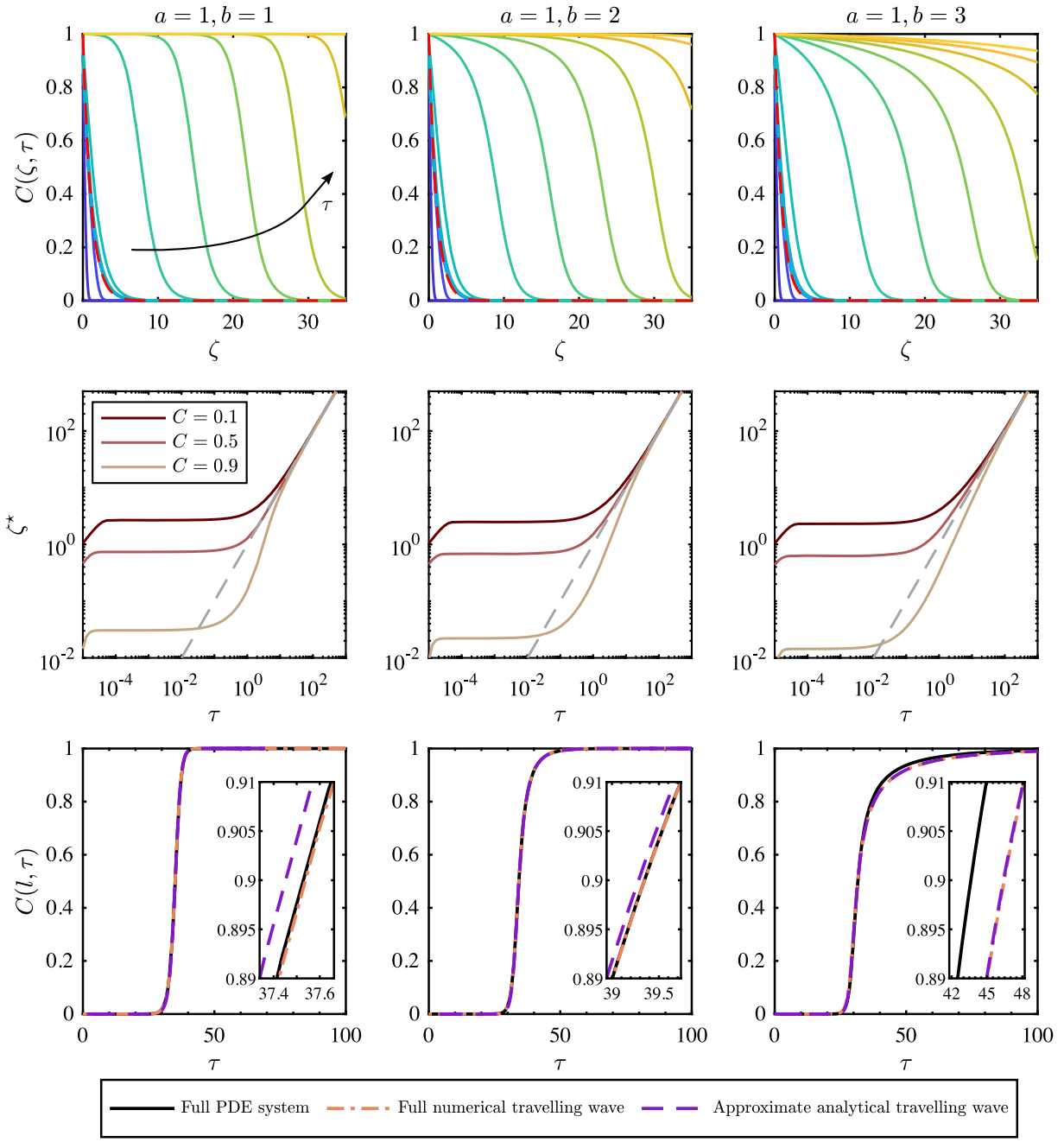

Fig. 4. Same as in Fig. 3 but with the following changes to parameter values: $\mu = 1.1$, $\mathrm{Pe}^{-1} = 0.1$, $\beta = 5$, $\mathrm{Da} = 2\alpha = 1 \times 10^{-5}$, $l = 35$ (first and third rows), $l = 500$ (second row) and, in the top row $\tau \in \{10^{-6}, 4.6 \times 10^{-6}, 2.2 \times 10^{-5}, 10^{-4}, 4.6 \times 10^{-4}, 2.2 \times 10^{-3}, 0.01, 0.046, 0.22, 1.0, 8.0, 15, 22, 29, 36, 43, 50\}$.

agreement between the three solutions for the two considered parameter sets. The analytical solutions can therefore be considered accurate and may be used to fit the experimental data in §4.

4. Discussion and results

In this section, we examine the behaviour of the analytical models developed in §3.4 and assess their accuracy in capturing the behaviour of two different data sets. In particular, we consider data from Sulaymon et al. [19] on the removal of the Mercury(II) ion, denoted Hg(II) (or, equivalently, Hg^{2+}) by modified activated carbon from distilled water, and data from Goeppert et al. [20] on carbon capture by fumed silica impregnated with polyethylenimine (PEI). In the former case, Sulaymon et al. [19] state that the activated carbon adsorbent grains are approximately spherical. In the latter case, the fumed silica is essentially a powder, so the

Table 2
Experimental parameters for the adsorption of Hg(II) by activated carbon as extracted from the column experiments detailed in [19]. The half-time $t_{1/2} := \tau_{1/2}\mathcal{T}$.

Extracted experimental parameters: column						
Parameter	Symbol	SI Units	Value			
Inlet concentration	c_{in}	mol/m^3	0.249			
Effective diffusivity	D	m/s^2	3.06×10^{-9}			
Interstitial velocity	v	m/s	1.19×10^{-3}			
Column length	L	m	0.05			
Cross section area	$\lvert W\rvert$	m^2	1.96×10^{-3}			
Bulk density	ρ_b	kg/m^3	784			
Column porosity	ϕ	-	0.601			
Particle porosity	ϕ_p	-	0.760			
Particle radius ($\times10^{-4}$)	R	m	1.03	1.90	3.08	3.89
Half-time	$t_{1/2}$	h	1.57	1.23	0.947	0.680
Adsorbed amount at equilibrium[a]	$\bar{m}_e$	mol/kg	0.0252	0.0198	0.0152	0.0108
Maximum adsorption possible[b]	$\bar{m}_{max}$	mol/kg	0.0482	0.0378	0.0291	0.0208

[a] Calculated via Equation (68).
[b] Calculated via $\mu\bar{m}_e$, with μ calculated using the isotherm data and model (the asymptote).

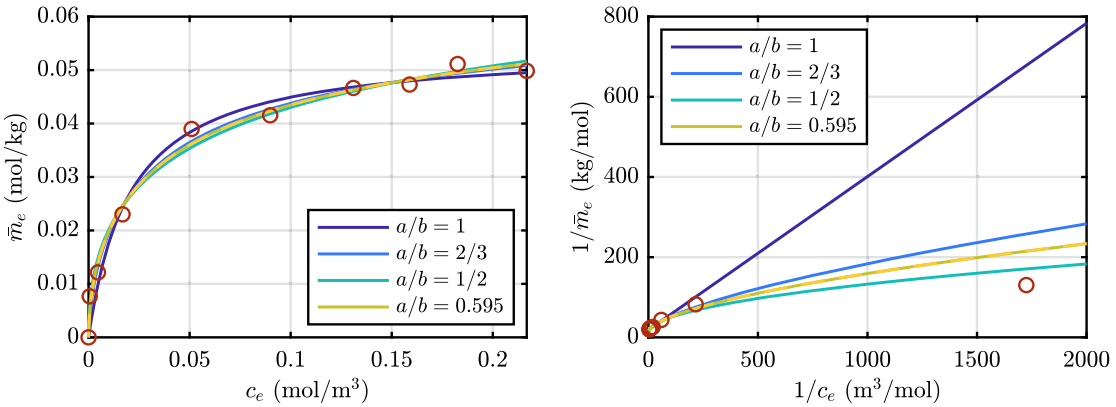

Fig. 5. Fitting of Sips isotherm (19) to the batch data of [21] for Hg(II) with average particle radius $R = 1.875\times10^{-4}$ m. We denote the concentration of Hg(II) at equilibrium as c_e.

geometry of the particles is assumed to be spherical. Therefore, throughout this section we assume that the column filters have a circular cross-section and that the porous grains are spherical; this assumption means that the specific surface $|\partial\omega|/|\omega| = 3/R$, where R is now the radius of the grain.

4.1. Removal of Hg(II) on activated carbon

Sulaymon et al. [19] investigate the removal by adsorption of various metallic ions from a water based solution by activated carbon. Here, we focus on one ion in particular, Hg(II). The experimental parameters as determined in Sulaymon et al. [19] are summarised in Table 2.

The amount of Hg(II) adsorbed at equilibrium, $\bar{m}_e$, has been calculated by integrating the area over the breakthrough curve via

$$\bar{m}_e \equiv (v\phi/(\rho_b L))\int_0^\infty (c_{in} - \bar{c})\,\mathrm{d}t. \tag{68}$$

Thus, the maximum adsorption is $\bar{m}_{max} \equiv \mu\bar{m}_e$. Using the data from the batch experiments in Yousif et al. [21], we take $\mu = 1.9125$. Note that the authors of Yousif et al. [21] are the same as in Sulaymon et al. [19] and consider the same experimental conditions but for batch (static) experiments.

Fig. 5 shows the fitting of the Sips isotherm (19) for various values of a/b, to the experimental data extracted from Yousif et al. [21], obtained by using the MATLAB Curve Fitting Toolbox. Note that, in Equation (19) c_e depends on a and b only through a term of the form a/b. Table 3 shows the calculated fitting parameters $\bar{m}_{max}$ and $\mathcal{K}$ and also the parameters measuring the goodness of fit (the sum of squared errors (SSE) and the R-squared value). Note that, as expected, the predicted $\bar{m}_{max}$ values are higher for the batch experiments than they are for the column experiments.

By considering a/b as another fitting parameter, we determine that $a/b = 0.595$ yields the best fit (the lowest SSE and the R-squared closer to one). However, according to the reaction (48), this has no clear physical significance. The most physically

Table 3
Sum of Squared Errors (SSE) and R-squared parameters obtained from fitting the Sips isotherm with various a and b to the equilibrium data of Yousif et al. [21]. $\bar{m}_{max}$ is taken from Yousif et al. [21], Fig. 1, for optimal pH.

Fitting parameters: isotherm					
Parameter	Units	$a/b=1$	$a/b=1/2$	$a/b=2/3$	$a/b=0.595$
$\bar{m}_{max}$	mol/kg	0.0543	0.0667	0.0902	0.0733
$\mathcal{K}^{1/b}$	m^3/mol	48.2	8.87	2.88	5.76
SSE	$(mol/kg)^2$	0.580×10^{-4}	0.294×10^{-4}	0.309×10^{-4}	0.281×10^{-4}
R-squared	-	0.983	0.991	0.991	0.992

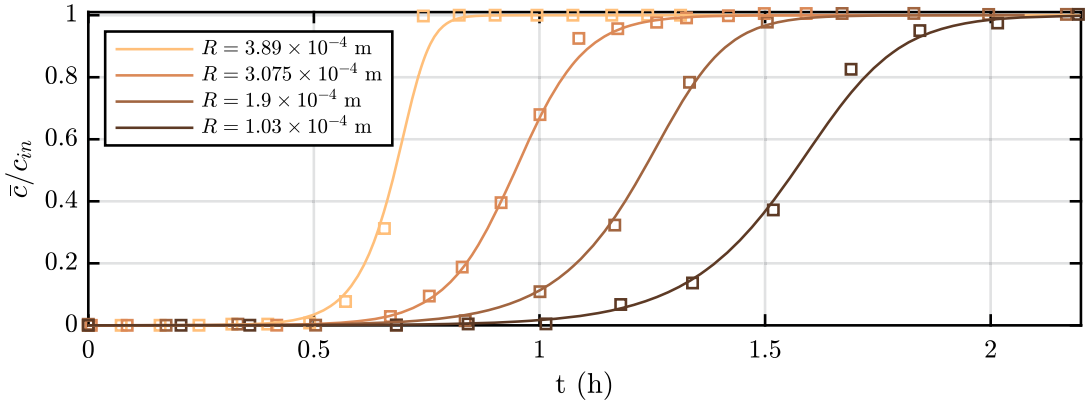

Fig. 6. Fitting of the approximate analytical breakthrough model (62) (corresponding to $a=1$ and $b=2$) to the experimental breakthrough data for Hg(II) adsorption onto activated carbon for four distinct particle sizes [19]. As R increases the colour transitions from dark brown to light orange.

reasonable combinations of a and b are $a/b=1, 1/2$, or $2/3$; out of these options $a/b=1/2$ and $2/3$ yield an R-squared value which is closest to unity. Despite the fact that $a/b=2/3$ yields a slightly lower SSE than $a/b=1/2$, the difference between these two options is sufficiently marginal that we cannot draw a conclusion on which is the correct choice. To better distinguish between these two cases, we consider small values of c_e (Fig. 5, right); from this we conclude that $a/b=1/2$ offers the best fit and thus best describes the kinetics of the Hg(II) adsorption. Using $a/b=1/2$, we find that $\bar{m}_{max}=0.0902$ mol/kg. To determine $\mu \equiv \bar{m}_{max}/\bar{m}_e$ we take the value $\bar{m}_e=0.0472$ mol/kg as reported in Yousif et al. [21] so that $\mu=1.9125$. Further, we take $\mu=1.9125$ to hold in the column studies.

The reaction orders $a=1, b=2$, which correspond to the ratio $a/b=1/2$, could be related to the oxidation state of Hg(II), which according to Fourier-transform infrared spectroscopy studies carried out by Sulaymon et al. [19], is complexed by H and O atoms of hydroxyl bonds in a cation exchange reaction.

On determining the kinetic orders $a=1$, $b=2$, we fit the analytical solution to the experimental breakthrough data [19]. The results are shown in Fig. 6. Since equations (61)–(65) are explicit in time, we used the MATLAB Curve Fitting Toolbox to fit the experimental times with those predicted by the model using the experimental breakthrough concentrations. The MATLAB routine uses the non-linear least squares method to obtain a feasible minimum. Each curve requires only two fitting parameters $\mathcal{T}=\bar{m}_e^{1-b}/(k_+ c_{in}^a)$ and $\beta = k_p|\partial\omega|\mathcal{T}\mathrm{Da}/(|\omega|\varphi)$. The results of the fitting are shown in Table 4. The SSE and R-squared values are also shown. In the literature it is common to present the error in terms of difference between c values rather than time hence the SSE and R-squared reported in Table 4 are calculated with the errors between concentrations.

The results in Fig. 6 and Table 4 show an excellent agreement between the model and the data with $a=1$, $b=2$. The values of k_+ and k_- generally increase with increasing particle size, while k_p decreases with increasing particle size. The equilibrium constant $\mathcal{K} \equiv k_+/k_-$ is constant at constant temperature, so the change in k_- is driven by that in k_+. Using these fitting parameters, we calculate the dimensionless values Pe^{-1}, Da and α. As shown in Table 4, we find $\mathrm{Pe}^{-1}=\mathcal{O}(10^{-3})$ and $\mathrm{Da}, \alpha=\mathcal{O}(10^{-3})$. This is consistent with the assumptions used to derive the travelling wave equations in §3.4.

The value of β is $\mathcal{O}(1)$ for all the particle sizes; this indicates that the effect of the particle size in the breakthrough curve is significant, as discussed in §2.5. The value of β also generally decreases as the particle radius (R) increases (see Table 4). The translation of the curves to the right as the particle size decreases shown in Fig. 6 indicates that the intra-particle diffusion is not the cause of the change in β, rather it is a result of the increase of the external specific surface when the column is filled with a greater number of small particles. Thus, the decrease of β in this model is indicative of the effect of particle size rather than the effect of intra-particle diffusion [4].

Table 4
Parameters obtained by fitting the approximate analytical breakthrough model (62) (corresponding to $a = 1$ and $b = 2$) to the experimental breakthrough data for Hg(II) adsorption onto activated carbon for four distinct particle sizes [19].

Dimensionless and fitting parameters: column					
Parameter	Units	Particle Radius (m)			
		1.03×10^{-4}	1.9×10^{-4}	3.075×10^{-4}	3.89×10^{-4}
$\mathcal{T}$	s	617	365	612	83.4
β	-	1.67	0.984	4.62	0.417
k_+	$m^3kg\ mol^{-2}s^{-1}$	0.258	0.556	0.431	4.434
k_-	$kg\ mol^{-1}s^{-1}$	0.0536	0.115	0.0894	0.920
k_p	m/s	1.84×10^{-5}	2.66×10^{-5}	9.29×10^{-5}	5.54×10^{-5}
$\mathcal{L}$	m	5.56×10^{-3}	4.18×10^{-3}	9.12×10^{-3}	1.74×10^{-3}
Pe^{-1}	-	4.64×10^{-4}	6.16×10^{-3}	2.82×10^{-4}	1.48×10^{-3}
Da	-	7.58×10^{-3}	9.66×10^{-3}	1.26×10^{-2}	1.76×10^{-2}
α	-	3.83×10^{-3}	4.87×10^{-3}	6.33×10^{-3}	8.88×10^{-3}
SSE	-	0.0077	0.0020	0.0043	0.0259
R-squared	-	0.9966	0.9993	0.9987	0.9934

Table 5
Experimental data extracted from Goeppert et al. [20].

Extracted experimental parameters: column						
Parameter	Symbol	SI Units	Value			
Inlet concentration	c_{in}	mol/m^3	0.0166			
Interstitial velocity	v	m/s	0.231			
Column length	L	m	0.100			
Cross section area	$\lvert W\rvert$	m^2	5.03×10^{-5}			
Bulk density	ρ_b	kg/m^3	541			
Column porosity[a]	ϕ	-	0.480			
Particle porosity	ϕ_p	-	0.416			
Effective diffusivity[b] ($\times10^{-4}$)	D	m/s^2	0.600	0.900	2.60	4.10
Particle radius ($\times10^{-4}$)	R	m	1.25	1.88	5.50	8.50
Half-time	$t_{1/2}$	h	10.7	11.9	12.1	14.0
Maximum adsorption possible	$\bar{m}_{max}$	mol/kg	1.66	1.73	1.75	1.92
Adsorbed amount at equilibrium	$\bar{m}_e$	mol/kg	1.61	1.68	1.70	1.86

[a] Porosity ϕ estimated with a column-to-particle diameter ratio $\in (4.7, 32)$ [30,31].
[b] Effective diffusivity coefficients approximated from experimental chart in Levenspiel [32].

4.2. Removal of CO_2 from air

Goeppert et al. [20] study the adsorption of carbon dioxide onto fumed silica impregnated with PEI. The addition of PEI to the silica improves the adsorption since CO_2 reacts with the primary and secondary amino groups in PEI. If the reaction occurs in a dry environment, two molecules of CO_2 react with the amine radicals to produce carbamate molecules on the surface of the adsorbent. However in the presence of water molecules, only one amine is needed to react with one molecule of CO_2 [20]. The experimental parameters as determined in [20] are summarised in Table 5.

Goeppert et al. [20] work with a range of particle diameters: <0.25 mm; 0.25–0.5 mm; 0.5–1.7 mm; and >1.7 mm. To calculate the radius used in Table 5, we take the average diameters for the intermediate values and 0.25, 1.7 mm for the extreme values. The isotherms are not provided in the paper but the adsorbed amount of contaminant at equilibrium is reported for each particle size and, for particles of diameters in the range 0.25–0.50 mm, the equilibrium amount is reported as a function of temperature. Given that all measurements were made with the same inlet concentration, the maximum adsorbed fraction, as well as other thermodynamic magnitudes (such as the enthalpy of adsorption) can be obtained using the Van't Hoff equation; this reads,

$$\mathcal{K} = A\exp\left(-\frac{\Delta H}{R_g T}\right), \tag{69}$$

where we recall that $\mathcal{K} = k_+/k_-$ is the equilibrium constant of the Sips isotherm ($m^{3a}mol^{-a}$), A is the pre-exponential factor in Van't Hoff equation ($m^{3a}mol^{-a}$), ΔH is the enthalpy of adsorption ($J\ mol^{-1}$), R_g the ideal gas constant ($8.314\ J\ K^{-1}mol^{-1}$) and T is the temperature (K). Thus, we have

$$\exp\left(\frac{\Delta H}{R_g T}\right) = A c_{in}^a \bar{m}_{max}^b \left(\frac{1}{\bar{m}_e} - \frac{1}{\bar{m}_{max}}\right)^b, \tag{70a}$$

which can be arranged into

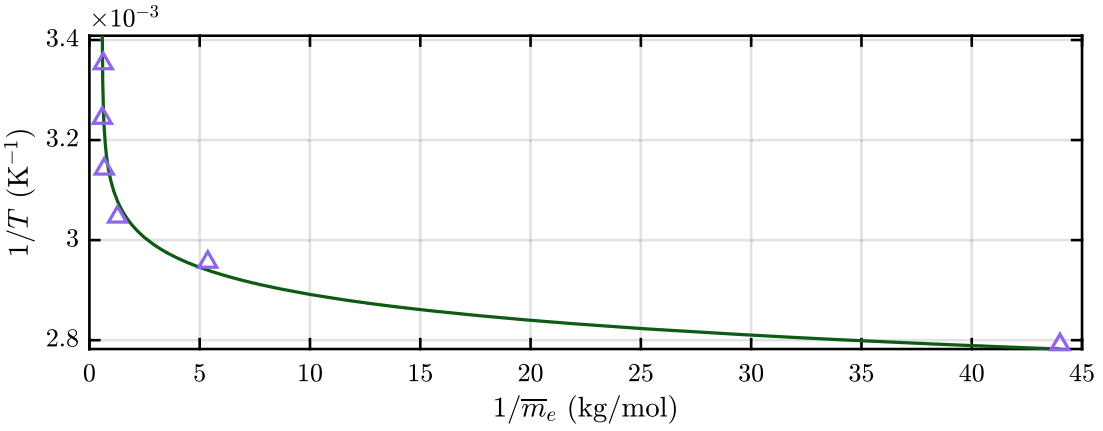

Fig. 7. Temperature versus adsorbed amount of CO_2 at equilibrium fitted with Equation (70b) for particles with diameters in the range 0.25–0.5 mm.

Table 6
Optimal parameters obtained via fitting of Equation (70b) to the experimental data of Goeppert et al. [20].

Parameter	Units	Value
$(R_g/\Delta H)\ln\left(Ac_{in}^a \bar{m}_{max}^b\right)$	K^{-1}	3.052×10^{-3}
$bR_g/\Delta H$	K^{-1}	-7.15×10^{-5}
$\bar{m}_{max}$	mol/kg	1.725

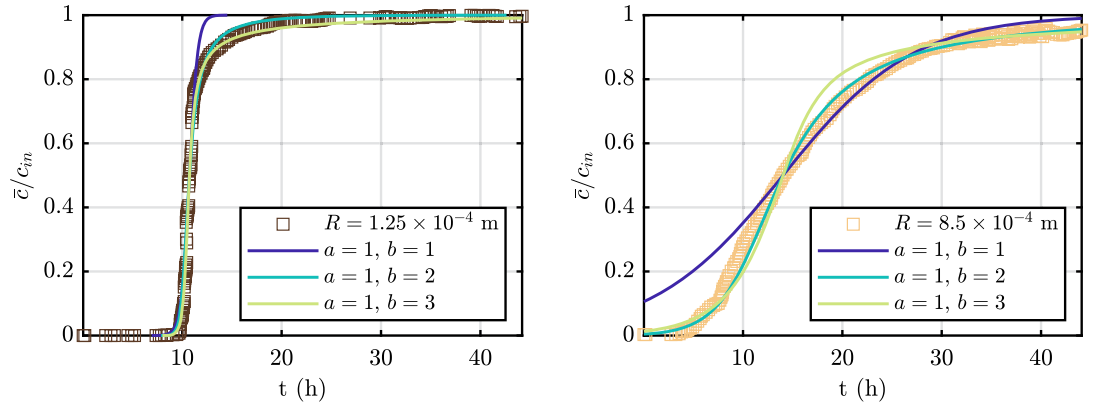

Fig. 8. Comparison of the breakthrough models (61) –(65) to the experimental data of Goeppert et al. [20]. Left: $R = 1.25\times10^{-4}$ m. Right: $R = 8.5\times10^{-4}$ m. Fitting parameters are presented in Table 7.

$$\frac{1}{T} = \frac{R_g}{\Delta H}\ln\left(Ac_{in}^a \bar{m}_{max}^b\right) + \frac{bR_g}{\Delta H}\ln\left(\frac{1}{\bar{m}_e} - \frac{1}{\bar{m}_{max}}\right). \tag{70b}$$

The fitting of Equation (70b) to the experimental data provided in Goeppert et al. [20] is shown in Fig. 7. This has been carried out using the MATLAB Curve Fitting Toolbox (see the codes in https://github.com/aguareles/Intra-particle-diffusion.git).

Table 6 shows the optimized fitting parameters. The value of $\bar{m}_{max}$ only applies to the particle size range 0.25–0.5 mm; for this particle size Goeppert et al. [20] determine $\bar{m}_{max} = 1.725$ mol/kg, hence $\mu = \bar{m}_{max}/\bar{m}_e = 1.03$. Since the maximum and the equilibrium adsorbed amount are considered to increase proportionally with increasing particle size we assume this value holds for all the particle sizes.

Note that the enthalpy of adsorption can only be obtained once the correct b is determined. In order to assess the form of the reaction (*i.e.* the values of the Sips exponents), we fit the breakthrough models (61) –(65) with the experimental data for the particle size of $R = 1.25\times10^{-4}$ m and $R = 8.5\times10^{-4}$ m (Fig. 8).

In Table 7 we present the fitted parameters ($\mathcal{T}$ and β), SSE and R^2 values for three a, b combinations and the two radii shown in Fig. 8. It is clear that the exponents $a = b = 1$ fit the experimental data the worst. Considering the smallest $R = 1.25\times10^{-4}$ m (Fig. 8, left), we note that both remaining combinations of exponents, that is, $a = 1, b = 2$ and $a = 1, b = 3$, offer a good fit. For $R = 1.25\times10^{-4}$ m, the lowest SSE and highest R-squared is obtained with the combination $a = 1, b = 3$; in this case the SSE for

Table 7
Sum of Squared Errors (SSE) and R-squared (R^2) parameters obtained from fitting the breakthrough models (61) – (65) to the experimental data of Goeppert et al. [20] with $R = 1.25 \times 10^{-4}$ m and $R = 8.5 \times 10^{-4}$ m.

Fitting parameters: column				
Radius (m)	Parameter	$a = b = 1$	$a = 1, b = 2$	$a = 1, b = 3$
1.25×10^{-4}	$\mathcal{T}$	1.49×10^{3}	1.08×10^{3}	2.83×10^{2}
	β	3.28×10^{5}	3.58×10^{5}	0.355
	SSE	0.542	0.295	0.0868
	R-squared	0.978	0.988	0.996
8.5×10^{-4}	$\mathcal{T}$	2.36×10^{4}	7.39×10^{3}	1.20×10^{3}
	β	8.20×10^{5}	5.44	0.101
	SSE	0.9839	0.0951	0.402
	R-squared	0.955	0.996	0.981

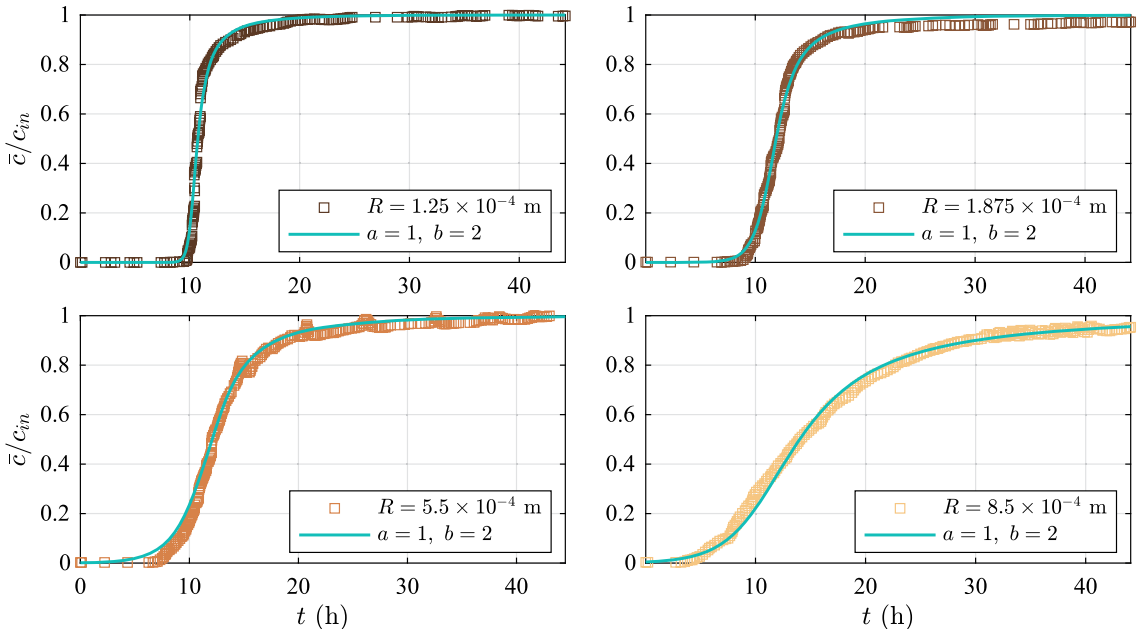

Fig. 9. Fitting of the breakthrough model (62) (corresponding to $a = 1$ and $b = 2$) to the experimental breakthrough data of Goeppert et al. [20] for a range of particle sizes, (a) $R = 1.25 \times 10^{-4}$, (b) $R = 1.875 \times 10^{-4}$, (c) $R = 5.5 \times 10^{-4}$, (d) $R = 8.5 \times 10^{-4}$.

$b = 3$ is ∼24% of the SSE for $b = 2$. However, this situation is reversed for the largest $R = 8.5 \times 10^{-4}$ m (Fig. 8, right), for which the combination $a = 1, b = 2$ provides a lower SSE, and a higher R-squared. For $R = 8.5 \times 10^{-4}$ m, from the consideration of Fig. 8, right, it is evident $a = 1, b = 2$ provides a significantly better fit. Aguareles et al. [13] established a correlation between the exponents $a = 1, b = 2$ and the kinetics of the reaction of CO_2 with the amine groups in PEI in small particles. Thus, using the insight provided by Aguareles et al. [13], and the fact that the sum of the SSEs for $b = 2$ is 0.39, while for $b = 3$ it is 0.487, we take the exponent values to be $a = 1$ and $b = 2$. Below, we consider the remaining breakthrough data reported by Goeppert et al. [20].

The fitting of the experimental breakthrough data with the model (62) is shown in Fig. 9. As before the only fitting parameters are $\mathcal{T}$ and β; these are presented in Table 8. The results shown in Fig. 9 and Table 8 demonstrate excellent agreement between the model and experimental data. The values of k_+, k_- and k_p clearly show an inverse relation with increasing particles size, with the exception of k_p for the largest particle. We hypothesise that this apparent inconsistency might be related to experimental noise.

In contrast to the Hg(II) breakthrough curves in the present case, the half-time ($t_{1/2} := \tau_{1/2}\mathcal{T}$) shows little variation but the average rate of change of the breakthrough curves decreases in magnitude with increasing particle size, i.e., the concentration at the outlet increases more slowly as the size of the adsorbent increases. This trend indicates that the increase in particle size is related to a more significant intra-particle diffusion. For the smallest radius, we see $\beta = \mathcal{O}(10^5)$, which indicates intra-particle diffusion effects are negligible (and the model reduces to that of Aguareles et al. [13]). However, as the particle size increases so that $\beta = \mathcal{O}(1)$, the intra-particle model applies. The excellent data fit verifies the suitability of the model for large particles. Finally, we note $\mathrm{Pe}^{-1} = \mathcal{O}(10^{-1})$ and $\mathrm{Da}, \alpha = \mathcal{O}(10^{-6})$, hence all dimensionless values are sufficiently small to justify the approximations made in §3.4.

Table 8
Parameters obtained from fitting the breakthrough model (62) to the experimental breakthrough data of [20], for four particle sizes.

Dimensionless and fitting parameters: column					
Parameter	Units	Particle Radius (m)			
		1.25×10^{-4}	1.88×10^{-4}	5.50×10^{-4}	8.50×10^{-4}
$\mathcal{T}$	s	1.08×10^{3}	1.66×10^{3}	2.45×10^{3}	7.39×10^{3}
β	-	3.58×10^{5}	0.856	0.565	5.43
k_+	$m^3kg\ mol^{-2}s^{-1}$	0.0348	0.0218	0.0145	0.00440
k_-	$kg\ mol^{-1}s^{-1}$	5.13×10^{-7}	3.21×10^{-7}	2.14×10^{-7}	6.48×10^{-8}
k_p	m/s	1.40×10^{3}	0.0340	0.00453	0.0244
$\mathcal{L}$	m	2.27×10^{-3}	3.36×10^{-3}	4.90×10^{-3}	1.31×10^{-2}
Pe^{-1}	-	0.114	0.116	0.230	0.131
Da	-	9.10×10^{-6}	8.77×10^{-6}	8.64×10^{-6}	7.90×10^{-6}
α	-	4.10×10^{-6}	3.95×10^{-6}	3.90×10^{-6}	3.56×10^{-6}
SSE	-	0.295	0.121	0.235	0.0951
R^2	-	0.988	0.995	0.992	0.996

5. Conclusions/future work

This work provides a mathematical model that accounts for the effect of the micro-structure of the adsorbent in adsorption column processes combined with a Sips equation for the adsorption rate. The model has been carefully derived and analysed and subsequently tested against experimental data. The main contributions of this work can be summarized in the following points:

1. A rigorous derivation of the model has been presented, indicating the assumptions made at every step. The model correctly captures the multiscale nature of the processes accounting for the advection-driven transport in the inter-particle region, the diffusion-driven transport in the intra-particle region, and the adsorption phenomenon at the adsorbent surface.
2. Adsorption kinetics have been modeled with a Sips sink term. This accounts for different possible combinations of partial orders of reaction and is able to describe both physisorption and chemisorption. The relation between the partial orders a and b is also linked to the adsorbent performance through the isotherm profile.
3. The existence of a solution using a travelling wave approximation has been discussed in terms of the relation between partial orders and the value of μ (the ratio of maximum to final adsorbed mass). Analytical solutions using this approach have been provided for the most common combinations of partial-orders with "favourable adsorption" ($a \leq b$), namely $a = b = 1$, $a = 1$ $b = 2$ and $a = 1$ $b = 3$.
4. The travelling wave solutions were compared with the numerical solution of the full mathematical model using different parameter values. The agreement between the two solution forms was excellent for all of the a, b combinations studied.
5. Finally, the analytical solutions have been tested against experimental data for column breakthrough curves for two different applications: Hg(II) adsorption on activated carbon from wastewater, and direct air CO_2 capture on PEI modified fumed silica. The agreement between the breakthrough data and the analytical solution was excellent in all cases using the model with $a = 1, b = 2$ and only two fitting parameters. The values $a = 1, b = 2$ can be directly related to the reaction mechanism, namely with the ion-exchange reaction of Hg(II) that depends on the valence of the metal, and the reaction between CO_2 and the amine groups in the PEI structure.
   The pattern observed in the fitted values with changing particle radius provides physical insights, and proves the suitability of the model to capture the effect of the decreasing specific surface and/or the increasing influence of intra-particle diffusion with increasing particle size.

For all the reasons listed above, we can conclude that this work presents a significant contribution to the understanding of column adsorption processes and the underlying physical and chemical mechanisms.

This work represents a starting point for future studies where the solution under different a, b configurations is assessed. This includes the study of adsorbate-adsorbent systems with unfavourable adsorption ($a > b$). In certain situations these cases may be of practical interest, for example in certain geographic locations where, due to expense or availability, only low quality filter materials are accessible [33,34]. Another possible future line of research related to this work is its extension to non-integer orders, since many processes actually consist of complex mechanisms or multiple reactions which may be approximated by global kinetics with fractional partial orders [35].

Declaration of competing interest

The authors declare that they have no known competing financial interests or personal relationships that could have appeared to influence the work reported in this paper.

Data availability

The codes are available online in https://github.com/aguareles/Intra-particle-diffusion.

Acknowledgements

This publication is part of the research projects PID2020-115023RB-I00 (funding M. Aguareles, T.G. Myers, M. Calvo-Schwarzwalder) financed by MCIN/AEI/ 10.13039/501100011033/. L.C. Auton and T.G. Myers acknowledge the CERCA Programme of the Generalitat de Catalunya for institutional support, their work was also supported by the Spanish State Research Agency, through the Severo Ochoa and Maria de Maeztu Program for Centres and Units of Excellence in R&D (CEX2020-001084-M). A. Valverde acknowledges support from the Margarita Salas UPC postdoctoral grants funded by the Spanish Ministry of Universities with European Union funds - NextGenerationEU. M. Aguareles acknowledges the support of the "consolidated research group" (Ref 2021 SGR01352) of the Catalan Ministry of Research and Universities. Open Access funding provided thanks to the CRUE-CSIC agreement with Elsevier.

Appendix A. Numerical scheme

Here, we discuss the numerical schemes in more detail.

A.1. Full PDE system

Spectral collocation methods involve discretising the solution domain into a set of N points (collocation points), defining a global function that interpolates the solution at these collocation points (the interpolant), and then approximating the derivatives of the solution as the derivatives of the interpolant. In a Chebyshev spectral collocation method, the collocation points are the N Chebyshev points $x_k \in [1,-1]$, which can be defined as [23]

$$x_k = \cos\left(\frac{(k-1)\pi}{N-1}\right), \quad k = 1,\dots,N. \tag{A.1}$$

The basis functions from which the interpolant is composed are then a set of N polynomials of degree $N-1$ satisfying the criterion that each is nonzero at exactly one distinct collocation point. Note that other definitions of the Chebyshev points are also commonly used (*e.g.*, [24]). For the definition (A.1), Weideman and Reddy [36] provide a suite of `MATLAB` functions that generate the Chebyshev points and differentiation matrices, and that perform interpolation.

We next outline the implementation of the numerical scheme; we express the system of equations (22) in vector notation via

$$\mathfrak{M}\frac{\partial \boldsymbol{Y}}{\partial \tau} = \boldsymbol{F}[\boldsymbol{Y}], \tag{A.2}$$

where $\boldsymbol{Y} := (C, C_p, m_p)^\intercal$ is the concatenated vector of the dependent variables, $\mathfrak{M}$ is a constant 3×3 mass matrix and where $\boldsymbol{F}$ is a continuous vector partial-differential operator in ζ. Below, we denote spatially discretised quantities with tildes; vectors and matrices are additionally in bold. Following the method of lines, we discretise ζ, C, C_p and m_p in space to have N elements each which we denote by $\tilde{\boldsymbol{C}}$, $\tilde{\boldsymbol{C}}_p$ and $\tilde{\mathfrak{M}}_p$. Concatenating $\tilde{\boldsymbol{C}}$, $\tilde{\boldsymbol{C}}_p$ and $\tilde{\boldsymbol{m}}_p$ produces a vector $\tilde{\boldsymbol{Y}}$ of length $3N$. Further we discretise $\mathfrak{M}$ into a $3N\times 3N$ constant mass matrix. Using the first and second order Chebyshev differentiation matrices of size $N\times N$, nested in matrices of size $3N\times 3N$ which are otherwise zero, we discretise the vector operator $\tilde{\boldsymbol{F}}$.

For $\tilde{\boldsymbol{C}}_p$ and $\tilde{\boldsymbol{m}}_p$ with $0\le\zeta\le l$ and for $\tilde{\boldsymbol{C}}$ with $0<\zeta<l$ we have a system of coupled ODEs in time. At $\zeta=0$ and $\zeta=l$, we enforce the spatially discretised boundary conditions on $\tilde{\boldsymbol{C}}$, (*cf.*, conditions (23a,b)), which are algebraic in τ. Thus the $3N-2$ differential equations and two algebraic equations which enforce the boundary conditions on $\tilde{\boldsymbol{C}}$, constitute a system of DAEs.

We express this system of DAEs using a mass matrix $\tilde{\mathfrak{M}}$, which is the Chebyshev spatial discretisation of $\mathfrak{M}$. The mass matrix pre-multiplies the time derivative $\partial\tilde{\boldsymbol{Y}}/\partial\tau$ and enables us to enforce the boundary conditions on $\tilde{\boldsymbol{C}}$ by setting the first and N^{th} rows of $\tilde{\mathfrak{M}}$ identically equal to zero. We integrate this system of DAEs in time in `MATLAB`® using `ode15s`.

We provide the solver with an analytical Jacobian

$$\tilde{\mathfrak{J}} := \frac{\mathrm{d}}{\mathrm{d}\tilde{\boldsymbol{Y}}}\left(\tilde{\boldsymbol{F}}(\tilde{\boldsymbol{Y}})\right). \tag{A.3}$$

The spatial discretisation has spectral accuracy, so the overall accuracy will be determined by the accuracy of the time-stepping performed by `ode15s`.

Fig. A.10 (left) shows the footprint or sparsity pattern of the Jacobian matrix $\tilde{\mathfrak{J}}$ for $N=11$ as defined in Equation (A.3).

A.2. Full system of travelling wave ODEs

Here, we show the analogous Jacobian but for full travelling wave system (Fig. A.10, right). The structural difference between Fig. A.10 left and right is that for the PDE we only have spatial derivatives for C, thus we only have the dense differentiation matrix in the top left corner, rather than for all three variables as in the ODE system. Note that the internal/boundary conditions are

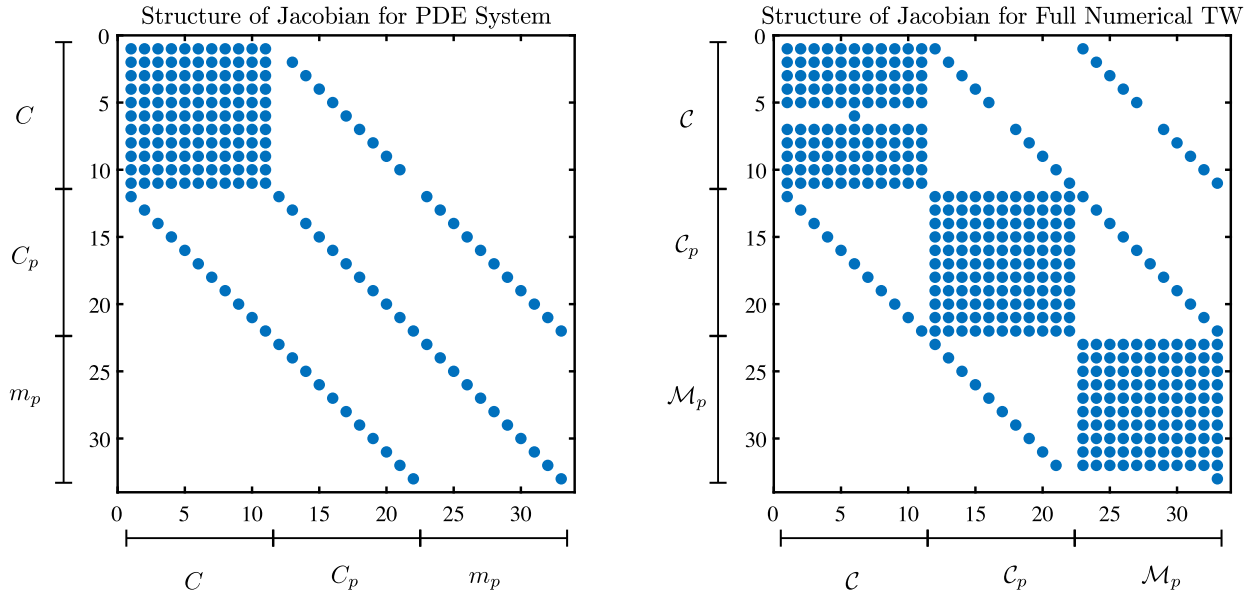

Fig. A.10. The footprint, or sparcity pattern for the analytically determined Jacobians used in the numerical schemes, for $N = 11$. ***Left***: Full PDE system. ***Right***: Full ODE system after travelling wave assumption.

enforced via putting the identity element in the intersection of the row and the column that correspond to that point— that is, for the internal condition the only entry in row $(N+1)/2$ is at column $(N+1)/2$, while for the boundary condition, the only entry in row $3N$ is at column $3N$. All codes are available in https://github.com/aguareles/Intra-particle-diffusion.git.

Appendix B. Proof of Proposition 1

We first provide two lemmas that will be used to prove Proposition 1:

Lemma 1. *Given $\beta, \mu \in \mathbb{R}$ such that $\mu > 1$ and $\beta > 0$, for any $a, b \in \mathbb{N}$, and for all $x \in [0,1]$ the equation*

$$\beta(x-y) = y^a(\mu - x)^b - (\mu-1)^b x^b, \tag{B.1}$$

(i) *implicitly determines a unique function $y(x) \in [0,1]$ such that $y(x)$ is continuously differentiable in the interval $[0,1]$.*
(ii) *if $a \le b$, then $0 < y(x) < x$.*

Proof. To prove the first statement for a fixed value $x \in (0,1)$ we define

$$p_1(y) = \beta(x-y), \quad p_2(y) = y^a(\mu-x)^b - (\mu-1)^b x^b,$$

and note that $p_1(y)$ is strictly decreasing while $p_2(y)$ is strictly increasing if $y \in (0,1)$. Further note that, $p_1(0) = \beta x > 0$ and $p_2(0) = -x^b(\mu-1)^b < 0$ if $x > 0$, while $p_1(1) = \beta(x-1) < 0$ and

$$p_2(1) = (\mu-x)^b - x^b(\mu-1)^b = (\mu-x)^b\left(1 - x^b\left(\frac{\mu-1}{\mu-x}\right)^b\right) > 0,$$

if $0 < x < 1$. Therefore, $p_1(y), p_2(y)$ have a unique intersection point, $y \in (0,1)$. Also, we note that if $x = 0$, Equation (B.1) reads

$$-\beta y = y^a \mu^b,$$

and the only solution in the interval $[0,1]$ is $y = 0$. When $x = 1$, Equation (B.1) reads

$$\beta(1-y) = y^a(\mu-1)^b - (\mu-1)^b,$$

whose only solution in $[0,1]$ is also $y = 0$. Finally, the regularity of $y(x)$ follows from the Implicit Function Theorem.

As for the second statement, we again use the monotonicity of $p_1(y)$ and $p_2(y)$ and note that $p_1(0) > 0$, $p_2(0) < 0$, $p_1(x) = 0$ and

$$p_2(x) = x^a(\mu-x)^b - x^b(\mu-1)^b = x^a(\mu-x)^b\left(1 - x^{b-a}\left(\frac{\mu-1}{\mu-x}\right)^b\right) > 0,$$

provided $b-a \geq 0$ and $x \in (0,1)$. This shows that in this case there is an intersection point y between zero and one and therefore, the solution $y(x)$ of $p(y)=0$ must be between 0 and x. □

Lemma 2. *Given $\mu \in \mathbb{R}$ such that $\mu > 1$, for any $a, b \in \mathbb{N}$ such that $a \leq b$, the only roots of the polynomial*

$$p(x) = x^a(\mu - x)^b - (\mu - 1)^b x^b, \tag{B.2}$$

in the interval $[0,1]$ are given by $x=0$ and $x=1$.

Proof. We note that $x=0$ is a root of $p(x)$. We then rewrite the polynomial (B.2) as

$$p(x) = x^a(\mu-1)^b \left[\left(\frac{\mu - x}{\mu - 1} \right)^b - x^{b-a} \right],$$

and define

$$\mathcal{P}_1(x) = \left(\frac{\mu - x}{\mu - 1} \right)^b, \qquad \mathcal{P}_2(x) = x^{b-a}.$$

If $a < b$, these polynomials satisfy,

$$\mathcal{P}_1(1) = \mathcal{P}_2(1) = 1 \qquad \mathcal{P}_1(0) = \left(\frac{\mu}{\mu - 1} \right)^b > 1 \qquad \mathcal{P}_2(0) = 0,$$

and therefore $x=1$ is another root of $p(x)$. The fact that $\mathcal{P}_1(x)$ is strictly decreasing and $\mathcal{P}_2(x)$ is strictly increasing between zero and one invalidates the possibility of finding any other root of $p(x)$ different than $x=0$ and $x=1$.

If $a=b$, $\mathcal{P}_2(x) \equiv 1$ and therefore, since $\mathcal{P}_1(x)$ is strictly decreasing in the interval $[0,1]$, the only intersection point between the two polynomials takes place at $x=1$. □

We now prove Proposition 1, which states:

Proposition 1. *Given $\mu, \beta, c_0 \in \mathbb{R}$ such that $\mu > 1$, $\beta > 0$, and $0 < c_0 < 1$, for any $a, b \in \mathbb{N}$ such that $a \leq b$, the initial value problem given by the equation*

$$\frac{\mathrm{d}C}{\mathrm{d}\eta} = -\beta \left(C - C_p(C) \right), \tag{B.3a}$$

along with the initial condition

$$C(0) = c_0, \tag{B.3b}$$

where $C_p(C)$ is implicitly determined by

$$\beta \left(C - C_p \right) = C_p^a (\mu - C)^b - (\mu - 1)^b C^b, \tag{B.3c}$$

is well posed and it has a unique decreasing solution, $C(\eta)$ satisfying

$$\lim_{\eta \to -\infty} C = 1, \quad \lim_{\eta \to \infty} C = 0. \tag{B.4}$$

Proof. Lemma 1 provides the existence of $C_p(C)$ as the unique continuously differentiable solution of Equation (B.3c),

$$\beta \left(C - C_p \right) = C_p^a (\mu - C)^b - (\mu - 1)^b C^b,$$

in the interval $[0,1]$. Therefore the initial value problem (B.3),

$$\frac{\mathrm{d}C}{\mathrm{d}\eta} = -\beta \left(C - C_p(C) \right),$$
$$C(0) = c_0,$$

is well posed and it has a unique solution for any initial value $c_0 \in (0,1)$. Note further that the equilibrium points of the polynomial (B.3a) satisfy $C = C_p$ and they are provided by the roots of the polynomial (B.2), so in particular they are independent of β. This means that the only equilibrium points in the interval $[0,1]$ are $C=0$ and $C=1$. Lemma 1 also states that if $C \in (0,1)$, then $0 < C_p < C$ which forces the solution of the initial value problem (B.3) to be strictly decreasing. Therefore C connects $C=1$ with $C=0$ and so the boundary conditions

$$\lim_{\eta \to -\infty} C = 1, \quad \lim_{\eta \to \infty} C = 0,$$

are satisfied. □

References

[1] G.S. Bohart, E.Q. Adams, Some aspects of the behavior of charcoal with respect to chlorine, J. Am. Chem. Soc. 42 (1920) 523–544.
[2] S. Li, S. Deng, L. Zhao, R. Zhao, M. Lin, Y. Du, Y. Lian, Mathematical modeling and numerical investigation of carbon capture by adsorption: literature review and case study, Appl. Energy 221 (2018) 437–449.
[3] T.G. Myers, Is it time to move on from the Bohart-Adams model for column adsorption?, Int. Commun. Heat Mass Transf. (Feb. 2024), submitted for publication, https://doi.org/10.2139/ssrn.4528144.
[4] A. Valverde, A. Cabrera-Codony, M. Calvo-Schwarzwalder, T.G. Myers, Investigating the impact of adsorbent particle size on column adsorption kinetics through a mathematical model, Int. J. Heat Mass Transf. 218 (2024) 124724.
[5] T.G. Myers, A. Cabrera-Codony, A. Valverde, On the development of a consistent mathematical model for adsorption in a packed column (and why standard models fail), Int. J. Heat Mass Transf. 202 (2023) 123660.
[6] T.G. Myers, F. Font, Mass transfer from a fluid flowing through a porous media, Int. J. Heat Mass Transf. 163 (2020) 120374.
[7] T.G. Myers, F. Font, M.G. Hennessy, Mathematical modelling of carbon capture in a packed column by adsorption, Appl. Energy 278 (2020) 115565.
[8] H. Patel, Characterization and adsorptive treatment of distillery spent wash using bagasse fly ash, Arab. J. Sci. Eng. 47 (2021) 5521–5531.
[9] I. Langmuir, The adsorption of gases on plane surfaces of glass, mica and platinum, J. Am. Chem. Soc. 40 (9) (1918) 1361–1403.
[10] R. Sips, On the structure of a catalyst surface, J. Chem. Phys. 16 (5) (1948) 490–495.
[11] R. Mondal, S. Mondal, K.V. Kurada, S. Bhattacharjee, S. Sengupta, M. Mondal, S. Karmakar, S. De, I.M. Griffiths, Modelling the transport and adsorption dynamics of arsenic in a soil bed filter, Chem. Eng. Sci. 210 (2019) 115205.
[12] S. Seidensticker, C. Zarfl, O.A. Cirpka, P. Grathwohl, Microplastic–contaminant interactions: influence of nonlinearity and coupled mass transfer, Environ. Toxicol. Chem. 38 (8) (2019) 1635–1644.
[13] M. Aguareles, E. Barrabés, T.G. Myers, A. Valverde, Mathematical analysis of a Sips-based model for column adsorption, Phys. D: Nonlinear Phenom. 448 (2023) 133690.
[14] C.E. Borba, E.A. da Silva, M.R. Fagundes-Klen, A.D. Kroumov, R. Guirardello, Prediction of the copper (II) ions dynamic removal from a medium by using mathematical models with analytical solution, J. Hazard. Mater. 152 (1) (2008) 366–372.
[15] T.L.P. Dantas, F.M.T. Luna, I.J. Silva, D.C.S. de Azevedo, C.A. Grande, A.E. Rodrigues, R.F.P.M. Moreira, Carbon dioxide–nitrogen separation through adsorption on activated carbon in a fixed bed, Chem. Eng. J. 169 (1) (2011) 11–19.
[16] M.S. Shafeeyan, W.M.A.W. Daud, A. Shamiri, N. Aghamohammadi, Modeling of carbon dioxide adsorption onto ammonia-modified activated carbon: kinetic analysis and breakthrough behavior, Energy Fuels 29 (10) (2015) 6565–6577.
[17] J.R.A. Pearson, A note on the “Danckwerts” boundary conditions for continuous flow reactors, Chem. Eng. Sci. 10 (1959) 281–284.
[18] Robert Osserman, The isoperimetric inequality, Bull. Am. Math. Soc. 84 (6) (1978) 1182–1238.
[19] A.H. Sulaymon, S.A. Yousif, M.M. Al-Faize, Competitive biosorption of lead Mercury chromium and arsenic ions onto activated sludge in fixed bed adsorber, J. Taiwan Inst. Chem. Eng. 45 (2) (2014) 325–337.
[20] A. Goeppert, H. Zhang, M. Czaun, R.B. May, G.K.S. Prakash, G.A. Olah, S.R. Narayanan, Easily regenerable solid adsorbents based on polyamines for carbon dioxide capture from the air, ChemSusChem 7 (5) (2014) 1386–1397.
[21] S.A. Yousif, A.H. Sulaymon, M.M. Al-Faize, Experimental and theoretical investigations of lead Mercury chromium and arsenic biosorption onto dry activated sludge from wastewater, Int. Rev. Chem. Eng. 5 (1) (2013) 30–40.
[22] P. Royer, C. Boutin, Time analysis of the three characteristic behaviours of dual-porosity media. I: fluid flow and solute transport, Transp. Porous Media 95 (2012) 603–626.
[23] R. Piché, J. Kanniainen, Solving financial differential equations using differentiation matrices, in: Proceedings World Congress on Engineering, vol. II, 2007, pp. 1016–1022.
[24] L.N. Trefethen, Spectral Methods in MATLAB, SIAM, 2000.
[25] T.I. Bjørnarå, S.A. Mathias, A pseudospectral approach to the McWhorter and Sunada equation for two-phase flow in porous media with capillary pressure, Comput. Geosci. 17 (2013) 889–897.
[26] L.C. Auton, C.W. MacMinn, From arteries to boreholes: transient response of a poroelastic cylinder to fluid injection, Proc. R. Soc. A 474 (2018) 20180284.
[27] L.C. Auton, C.W. MacMinn, From arteries to boreholes: steady-state response of a poroelastic cylinder to fluid injection, Proc. R. Soc. A 473 (2017) 20160753.
[28] R. Piché, J. Kanniainen, Matrix-based numerical modelling of financial differential equations, Int. J. Math. Model. Numer. Optim. 1 (1–2) (2009) 88–100.
[29] W.L. McCabe, J.C. Smith, P. Harriott, Unit Operations of Chemical Engineering, fifth edition, McGraw-Hill, Inc., ISBN 978-0-070-44844-5, 1993.
[30] H.K. Chan, Densest columnar structures of hard spheres from sequential deposition, Phys. Rev. E 84 (2011) 050302.
[31] A. Mughal, H.K. Chan, D. Weaire, S. Hutzler, Dense packings of spheres in cylinders: simulations, Phys. Rev. E 85 (2012) 051305.
[32] O. Levenspiel, Chemical Reaction Engineering, third edition, John Wiley & Sons, Inc, 1999.
[33] B. Bishayee, B. Ruj, S. Nandi, R.P. Chatterjee, A. Mallick, P. Chakraborty, J. Nayak, S. Chakrabortty, Sorptive elimination of fluoride from contaminated groundwater in a fixed bed column: a kinetic model validation based study, J. Indian Chem. Soc. (ISSN 0019-4522) 99 (1) (2022) 100302.
[34] L.C. Auton, M. Martínez-I-Ávila, S.S. Ravuru, S. De, T.G. Myers, A. Valverde, Mathematical model for fluoride-removal filters, in: Progress in Industrial Mathematics at ECMI 2023, Springer International Publishing, 2024, in press, https://doi.org/10.48550/arXiv.2312.03547.
[35] T. Yakabe, G. Imamura, G. Yoshikawa, N. Miyauchi, M. Kitajima, A.N. Itakura, 2-step reaction kinetics for hydrogen absorption into bulk material via dissociative adsorption on the surface, Sci. Rep. (ISSN 2045-2322) 11 (2021) 18836.
[36] J.A.C. Weideman, S.C. Reddy, A MATLAB differentiation matrix suite, ACM Trans. Math. Softw. 26 (4) (2000) 465–519.